iScience

CellPress
OPEN ACCESS

Article

Heterocellular spheroids of the neurovascular blood-brain barrier as a platform for personalized nanoneuromedicine

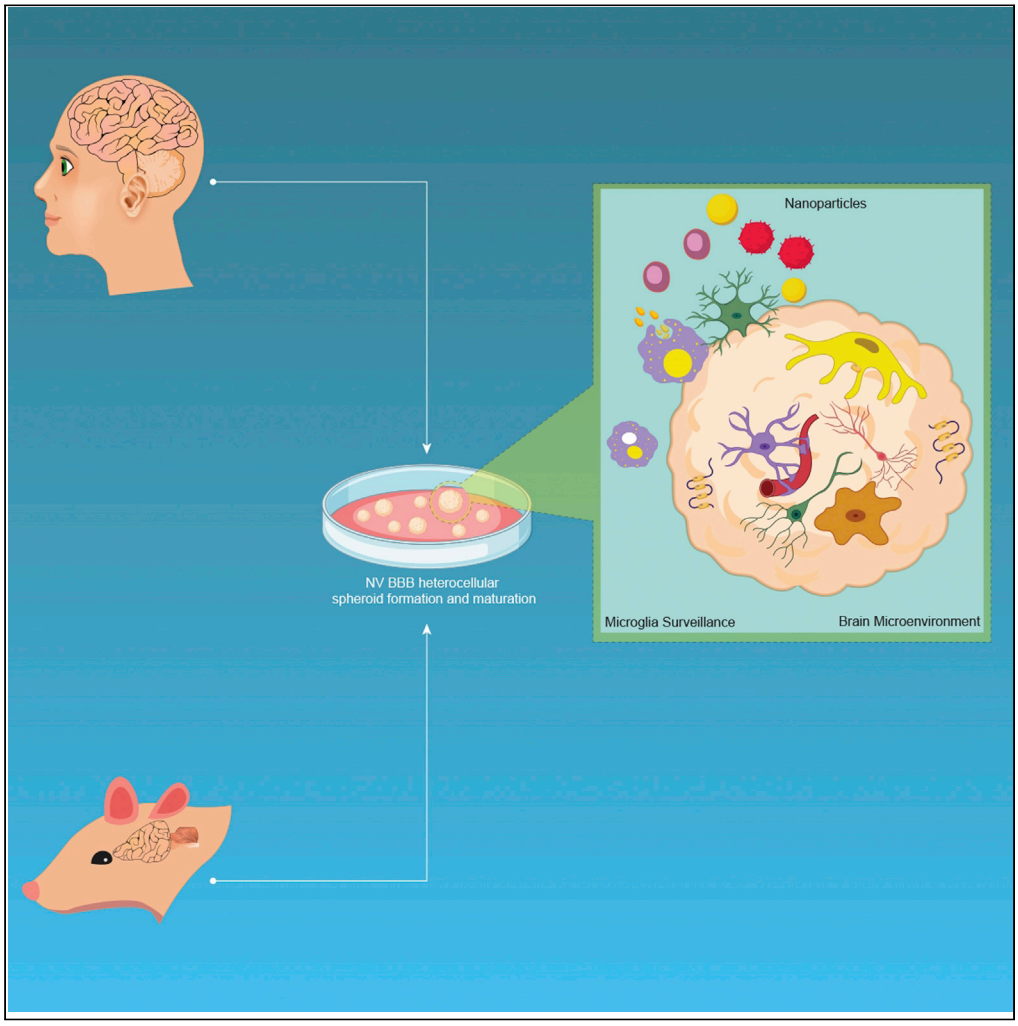

Murali Kumarasamy, Alejandro Sosnik

sosnik@technion.ac.il, alesosnik@gmail.com

HIGHLIGHTS

Heterocellular spheroids of the NVU are biofabricated by a simple method

Heterocellular spheroids express key structural and functional proteins of the BBB

RNA-Seq analysis confirmed high expression of endothelial cell-specific genes

Nanoparticles enter the spheroid, likely by activated microglia and astrocytes

Kumarasamy & Sosnik, iScience *24*, 102183 March 19, 2021
https://doi.org/10.1016/j.isci.2021.102183

iScience

CellPress
OPEN ACCESS

Article

Heterocellular spheroids of the neurovascular blood-brain barrier as a platform for personalized nanoneuromedicine

Murali Kumarasamy[1] and Alejandro Sosnik[1,2,*]

SUMMARY

Nanoneuromedicine investigates nanotechnology to target the brain and treat neurological diseases. In this work, we biofabricated heterocellular spheroids comprising human brain microvascular endothelial cells, brain vascular pericytes and astrocytes combined with primary cortical neurons and microglia isolated from neonate rats. The structure and function are characterized by confocal laser scanning and light sheet fluorescence microscopy, electron microscopy, western blotting, and RNA sequencing. The spheroid bulk is formed by neural cells and microglia and the surface by endothelial cells and they upregulate key structural and functional proteins of the blood-brain barrier. These cellular constructs are utilized to preliminary screen the permeability of polymeric, metallic, and ceramic nanoparticles (NPs). Findings reveal that penetration and distribution patterns depend on the NP type and that microglia would play a key role in this pathway, highlighting the promise of this platform to investigate the interaction of different nanomaterials with the central nervous system in nanomedicine, nanosafety and nanotoxicology.

INTRODUCTION

Neurological disorders (NDs) cause approximately 17% of the deaths worldwide and an enormous economical and societal burden (Group, 2017; Kaji, 2019; DiMasi et al., 2010). A major limitation in the treatment of NDs is that most drugs do not cross the blood-brain barrier (BBB) (Furtado et al., 2018). The BBB is formed by tightly bound endothelial cells and is an essential part of the neurovascular unit (NVU), a complex anatomical and functional heterocellular structure comprising a basal lamina covered with pericytes, smooth muscle cells, neurons, glia cells, an extracellular matrix (ECM), as well as a number of different neural stem/progenitor cells (Abbott, 2013; Netto et al., 2018; Sivandzade and Cucullo, 2018; Tam and Watts, 2010; Walchli et al., 2015). Understanding the central nervous system (CNS) pathways in health and disease, as well as the evaluation of new neurotherapeutics, has been challenging due to the complexity of the NVU (Paşca, 2018).

The use of nanotechnology to improve the delivery of neurotherapeutics to the CNS, a field coined nanoneuromedicine, has emerged as one of the most dynamic research areas in nanomedicine (Kreuter, 2014; Saraiva et al., 2016; Tang et al., 2019). Different strategies have been investigated to surpass the BBB by systemic (e.g., intravenous) and local (e.g., nasal) administration routes (Kreuter, 2014; Saraiva et al., 2016; Tang et al., 2019; Uchegbu et al., 2019). More recently, nanotoxicology has devoted efforts to develop reliable models to assess the detrimental interaction of different nanomaterials with the CNS upon intended or unintended exposure (Fadeel, 2019; Feng et al., 2015; Yang et al., 2010).

The systematic investigation of the biocompatibility, safety, permeability, and efficacy of nanoneuromedicines remains mostly limited to *in vivo* experiments. Rat and mouse have been the leading animal models in biomedical research and extensively used to model different neurodegenerative diseases (Dawson et al., 2018). Rats are similar to human in six isoforms of the tau protein and have been utilized as a preclinical model in Alzheimer disease (Hanes et al., 2009). However, the complex physiology of animal models challenges the conduction of permeability and mechanistic studies to understand the transport of nanoparticles (NPs) into the CNS (Esch et al., 2015).

[1]Laboratory of Pharmaceutical Nanomaterials Science, Department of Materials Science and Engineering, Technion-Israel Institute of Technology, De-Jur Bldg. Office 607, Technion City, 3200003 Haifa, Israel

[2]Lead contact

*Correspondence: sosnik@technion.ac.il, alesosnik@gmail.com

https://doi.org/10.1016/j.isci.2021.102183

Endothelial cell monolayers (e.g., hCMEC/D3 cell line) cultured on semipermeable membrane well plates have been the most commonly used *in vitro* model of the BBB (Naik and Cucullo, 2012). They use user-friendly setups, are scalable, and enable high-throughput screening. However, they cannot mimic the complex 3D cellular structure, the physiological microenvironment, and the cellular phenotype and homotypic and heterotypic cell-cell interactions in the NVU (Rommerswinkel et al., 2014). In addition, the formation of junctions that control paracellular transport is suboptimal (Biemans et al., 2017), and they exhibit effects that hinder cell growth, especially at the plate edges, which artificially increases the permeability. The development of 3D cell culture models has gained attention to investigate the transport of different neurotherapeutics into the brain (Bergmann et al., 2018; Bhalerao et al., 2020; Cho et al., 2017; Urich et al., 2013). Over the last century, the term "organoid" has been used to name different types of 3D cell aggregates and cultures, small tissue fragments taken from organs, and other associated cellular structures that closely model the cellular architecture of organs *in vivo* (Simian and Bissell, 2017). de Souza defined an organoid as a 3D multicellular tissue construct that mimics in structure and function the *in vivo* organ and can be used to study aspects of that organ *in vitro* (Author Anonymous, 2018). Fujii and Sato defined organoids as any heterocellular structure that can be reproducibly fabricated from somatic tissues or pluripotent stem cells, can self-assemble through homotypic and heterotypic cell-cell and cell-ECM communications, and have some features of the counterpart organs (Fujii and Sato, 2021). Bergmann et al. called BBB organoids to cellular structures produced without using stem cells (Bergmann et al., 2018). Some consensus exists to define an organoid exclusively when it is produced from pluripotent stem cells (this is the more orthodox definition) (Simian and Bissell, 2017), while those obtained from differentiated cells are called spheroids or assembloids when they combine different cell types. Regardless of the cell source (differentiated or stem cells), spheroids and organoids usually share two fundamental features: (i) they are formed by cellular self-assembly (and can be called assembloids) and (ii) they display some of the key features of the organ that they mimic. Organoids and spheroids represent a valuable tool to investigate pathophysiological pathways in the CNS (Amin and Paşca, 2018). Advantages of these 3D cellular constructs include easy and reproducible culture, miniature scale, small reagent volumes, low relative cost, reproducibility, and scalability. Furthermore, they reduce animal experimentation (Rossi et al., 2018). In the case of the NVU-BBB, most models are based on one-cell or three-cell cultures and fail to fully recreate its physiology (Cullen et al., 2019; Lee et al., 2017; Papaspyropoulos et al., 2020). One often missing cell type in these models is the so-called "third element" of the CNS, which is in fact resident macrophages (microglia) that constitute 10–15% of the total cells in the brain (Szepesi et al., 2018). We recently reported on the possible role of olfactory microglia in the nose-to-brain transport of different nanomaterials (Kumarasamy and Sosnik, 2019). This mechanism might be also exploited by pathogens such as the coronavirus disease 2019 to enter the CNS through the olfactory epithelium (Cheng et al., 2020; Meinhardt et al., 2020). In addition, glial cells (e.g., astrocytes), microglia, and neurons are actively involved in neuro-hemostasis and regulate the transmission of electrical signals in the brain (Heide et al., 2018; Hubbard et al., 2015; Koo et al., 2019; Park et al., 2018). Despite the recent advances in the development of BBB spheroids and organoids, they usually lack essential components of the BBB cellular milieu, including microglia, six distinct cortical layers, and endothelial vasculature. Moreover, the limited formation of microglia and mature neurons limits its utility for specific *in vitro* ND models. Thus, the application of these simplified 3D models to understand how different neurotherapeutics in general and nanoneuromedicines in particular are transported across the BBB and interact with phagocytic cells likely involved in their uptake and clearance remains a significant scientific challenge (Bhalerao et al., 2020; Paşca, 2018). In this scenario, the development of more robust, predictive, and cost-effective *in vitro* models that recapitulate better the complex cell-cell interactions in the BBB and the NVU function is called for.

In this work, we investigate a heterocellular spheroid comprising human brain microvascular endothelial cells (the hCMEC/D3 cell line), human brain vascular pericytes (hBVPs) and human astrocytes (hAs) combined with primary neurons and microglia isolated from neonate rats that were biofabricated by cell self-assembly and without the use of an ECM such as Matrigel. The structure of the constructs and the presence of homotypic (e.g., neuron-neuron) and heterotypic (e.g., endothelial cell-astrocyte) cell-cell interactions is characterized through the integration of confocal laser scanning fluorescence microscopy (CLSFM), light sheet fluorescence microscopy (LSFM), and scanning transmission electron microscopy (STEM) (Lazzari et al., 2019; Wilt et al., 2009). In addition, the upregulation of selected key BBB-related genes that code for tight junction proteins, solute carriers (SLCs), transporters of the ATP-binding cassette superfamily (ABCs), metabolic enzymes, and proteins of the basal membrane (BM) are screened by western blotting, RNA sequencing (RNA-Seq), and gene expression by quantitative polymerase chain reaction analysis. Finally, these heterocellular spheroids

were used to preliminarily characterize the permeability of different polymeric, metallic, and ceramic NPs. Overall results support the promise of this simple and scalable platform to investigate the interaction of nanomaterials with the BBB in nanoneuromedicine, nanosafety and nanotoxicology.

RESULTS AND DISCUSSION

Establishment and structural characterization of the neurovascular BBB

Heterocellular neurovascular 3D constructs are one of the most promising surrogate *in vitro* models in translational nanoneuromedicine, overcoming some of the shortcomings of monocellular 2D and 3D models (Peng et al., 2018). However, they do not incorporate microglia cells, which mediate immune responses in the CNS by acting as macrophages and clearing cellular debris, dead neurons, and taking up foreign particles. In addition, they usually require complex fabrication procedures.

In previous studies, we used BBB endothelial and olfactory neuroepithelial cells isolated from adult and neonate rat to study the compatibility and endocytosis of different polymeric NPs (Izak-Nau et al., 2014; Kumarasamy and Sosnik, 2019; Murali et al., 2015). The aim of the present work was to extend these investigations and to develop a platform of heterocellular spheroids that form by self-assembly and mimic the tightness of the BBB endothelium as a tool to assess the interaction of different types of nanomaterials with the BBB *in vitro* as a preamble to preclinical studies in relevant animal models.

Almost all the human genes associated with neurological diseases find a counterpart in the rat genome, and they appear highly conserved. There are 280 large gene regions called synteny blocks with chromosomal similarities between both species (Gibbs et al., 2004). Primary human microglia cells were not available, and we anticipated that the use of immortalized human microglia cell lines in which the endocytotic phenotype might have undergone alterations was of more limited physiological relevance than combining interspecies primary cells to produce our spheroids. For instance, recent studies have pointed out that microglia cell lines differ both genetically and functionally from primary microglia cells and *ex vivo* microglia (Das et al., 2016; Melief et al., 2016). Human and rat genomes show similarities (Gibbs et al., 2004), and studies demonstrated the potential of interspecies heterocellular spheroid models (Yang et al., 2019; Yip and Cho, 2013). In this work, we used a simple self-assembly method without ECM to biofabricate spheroids that combine three human cell types, namely hCMEC/D3, hBVPs, and hAs, and incorporated two primary rat cell types: (i) neurons that form synapses and neuronal networks and (ii) microglia cells involved in the uptake and clearance of particulate matter (Figure 1A; Video S1).

Before biofabrication, we characterized the five different neural tissue cell types by immunocytochemical staining. hCMEC/D3 cells are derived from human temporal lobe endothelial microvessels and produce two characteristic proteins of adherens and tight junctions, vascular endothelium (VE)-cadherin and claudin-5 (CLDN5), respectively (Figure 1B). Primary hAs express the filament protein glial fibrillary acidic protein (GFAP, Figure 1C) and hBVPs the neuron-glial antigen-2 (NG2) proteoglycan (Figure 1D). Primary neurons (Figure 1E) and microglia (Figures 1F and 1G) from neurogenic and non-neurogenic regions of neonate rat brains express βIII-tubulin, which is a microtubule element almost exclusive of neurons, and ionized calcium-binding adapter molecule-1/allograft inflammatory factor-1 (Iba-1/AIF-1) and inducible nitric oxide synthase (iNOS), which are overexpressed in classically activated microglia (M1 phenotype) that protect against nanoparticulate matter (Liu et al., 2012). Primary neurons are also positive for microtubule-associated protein-2 (MAP-2, data not shown). In these experiments, microglia changed the morphology from ramified characteristic of quiescent cells to a more flattened macrophage-like one (Figures 1F and 1G).

We characterized the interaction of rat microglia and hCMEC/D3 in 2-cell spheroids by looking at changes in cell density. Results indicated that no detrimental interspecies interactions (Levine and Grabel, 2017; Masaki and Nakauchi, 2017) such as cell death take place (Figure S1; Video S2).

After characterization of the individual cells, we used them to biofabricate heterocellular spheroids that resemble the complex BBB structure and utilized them to preliminarily assess the permeability and uptake of different types of NPs. We hypothesized that the phenotype of hCMEC/D3 in heterocellular constructs will mimic better their physiology and function of the BBB. To serve as a high-throughput screening tool in nanoneuromedicine, the biofabrication process needs to be simple, cheap, reproducible, robust, and eventually scalable.

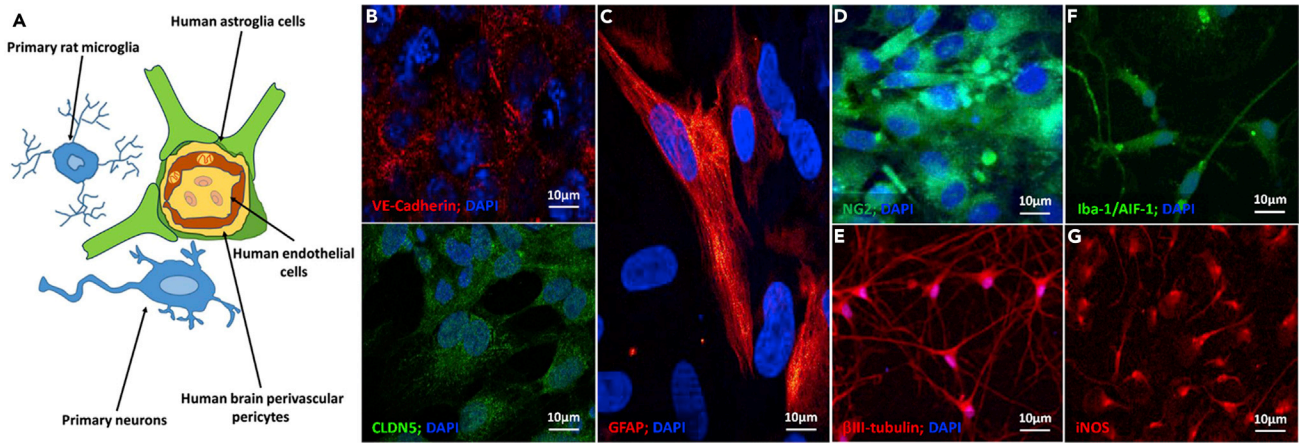

Figure 1. Immunocytochemical characterization of human and rat cells used in the biofabrication of heterocellular spheroids cultured in flat well plates

(A–G) (A) Scheme of the neurovascular units and (B–G) CLSFM micrographs of (B) hCMEC/D3 endothelial cells cultured on collagen-coated glass coverslips and their specific VE-cadherin (red) and CLDN5 (green) staining, (C) GFAP-positive primary hAs, (D) NG2-positive hBVPs (green), (E) βIII-tubulin-positive primary rat neurons (red), (F) Iba-1/AIF-1-positive primary rat microglia, and (G) iNOS-positive primary rat microglia. Cell nuclei in (B–F) are stained with 4′,6-diamidino-2-phenylindole (DAPI, blue).

For this, we mixed all the cell types at a hCMEC/D3:hAs:hBVPs:primary rat neurons:primary rat microglia ratio of 4:2:1:1:1 that recapitulates the cellular composition of the NVU (Zlokovic, 2008) and cultured them on agarose gel or round bottom well plates (see Methods section). After 2–3 days of incubation, spherical cell aggregates formed, and at day 5, they were fully characterized (Figure 2). 3D cultures were small spherical bodies with radially distributed cells, whereas monocultures in flat well plates exhibited enlarged cell bodies with less and short processes.

Cell viability in 5-cell spheroids after re-suspension was qualitatively assessed by using the LIVE/DEAD (calcein *O,O′*-diacetate tetrakis(acetoxymethyl) ester (calcein AM)/propidium iodide) assay and CLSFM. Most cells remained alive, confirming that the manipulation of the spheroids does not substantially affect cell viability and the absence of detrimental interspecies interactions that might lead to massive cell death (Figure S2) (Levine and Grabel, 2017; Masaki and Nakauchi, 2017). In addition, we estimated the relative fluorescence intensity of live and dead cells in a 5-cell spheroid by using ImageJ software. The intensity of calcein AM-stained cells was ~12-fold greater than that of the cells stained with propidium iodide, confirming the very good cell viability in the spheroids and the compatibility of the biofabrication process.

Upon production, spheroids were immunostained to reveal the cellular architecture by CLSFM (Figure 3). hCMEC/D3 endothelial cells together with pericytes appeared to form a surface monolayer tightly encasing the rest of the cells in the bulk of the 3D construct, and they expressed VE-cadherin (Figures 3A and 3B) and CLDN5 (Figure 3B) which are characteristic of adherens and tight junctions, respectively. These junctions play a key role in controlling paracellular transport across the BBB. In addition, they showed a strong immunostaining for GFAP (Figure 3C) that is characteristic of hAs, the NG2 proteoglycan of mature hBVPs (Figure 3D), βIII-tubulin (Figure 3E) and MAP-2 (Figure 3F) of primary rat neurons, and Iba-1/AIF-1 of primary rat microglia (Figure 3G). Microglial processes at the neuro-glia junctions could potentially monitor and protect neuronal functions.

Previous experiments demonstrated that CLSFM is not the most appropriate technique to monitor the inner cellular structure and the diffusion of fluorescently labeled NPs into the spheroids because it only allows us to scan a Z-stack depth of 100 µm. Imaging in deeper layers is time consuming and not feasible. The visualization of the whole heterocellular spheroid could be conducted more efficiently and in a short time by 3D tomography by using LSFM that enables the detection of fluorescence signals and the imaging of the sample as deep as 1 mm and thus of the cellular construct core (Albert-Smet et al., 2019; Lazzari et al., 2019). LSFM confirmed that our spheroids are a solid cellular structure (Figure S3). These results also confirmed that the cell density is conserved, in good agreement with the good cell viability (Figure S2). hCMEC/D3 endothelial cells cover almost completely and uniformly the spheroid surface, forming adherens junctions that are a fundamental

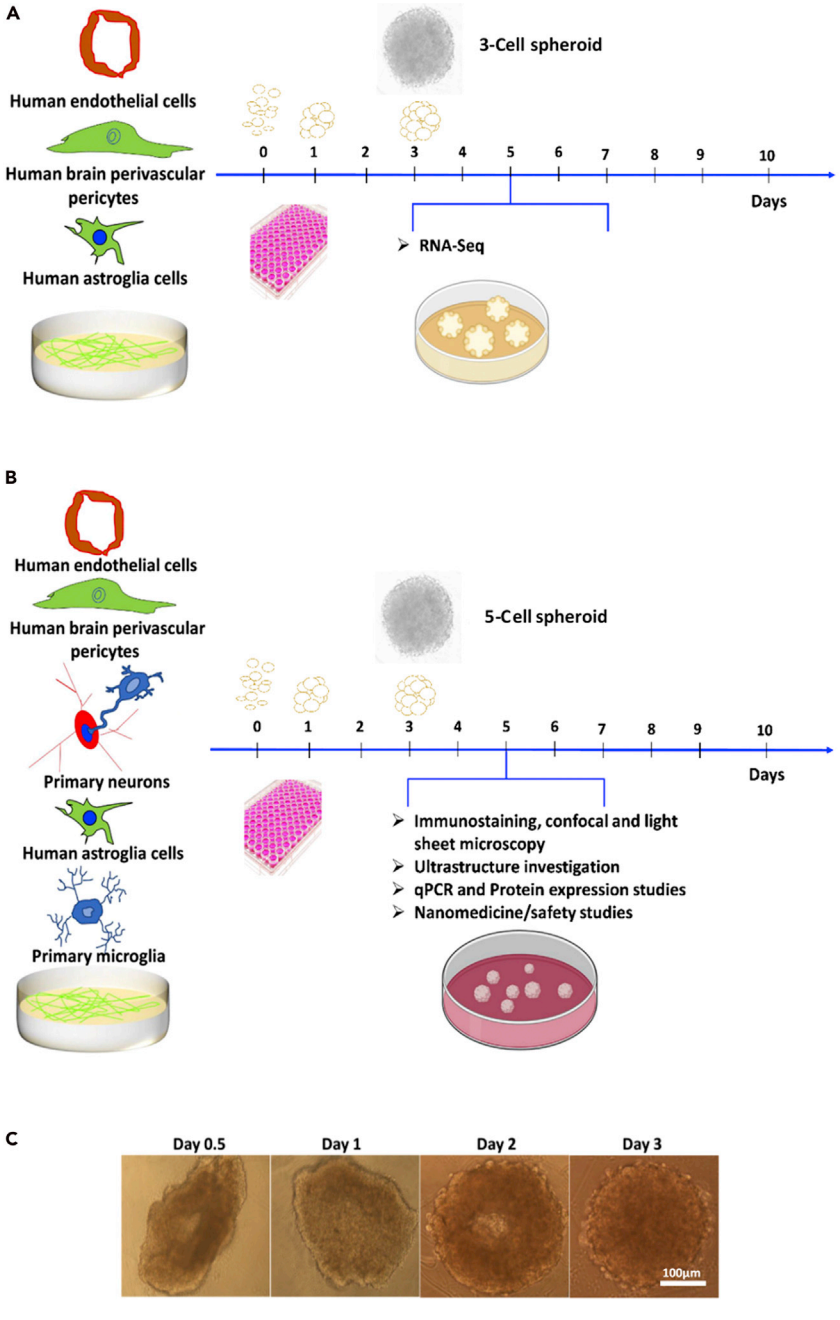

Figure 2. Biofabrication and characterization of 3-cell and 5-cell spheroids

(A and B) Scheme to produce (A) 3-cell and (B) 5-cell spheroids.

(C) Spherical 5-cell heterocellular spheroids formed within 2–3 days and were fully characterized at day 5.

structure to govern the permeability into the CNS (Figures 3H–3J). This observation was confirmed by CLSFM (Figure S4). In addition, microglia cells express Iba-1/AIF-1 (Figures 3J and 3K), a microglia/macrophage-specific Ca^{2+}-binding protein that participates in membrane ruffling and phagocytosis in activated microglia (Ohsawa et al., 2004). The staining of AQP4 (Figure 3L) and GFAP (Figure 3M) confirmed the presence of abundant filamentous bundles characteristic of hAs in the spheroid core.

Perivascular regions are also essential to mimic the physiology and function of the BBB along with the vascular endothelial barrier and astrocytic endfeet. For instance, astrocytes restore their phenotype in a

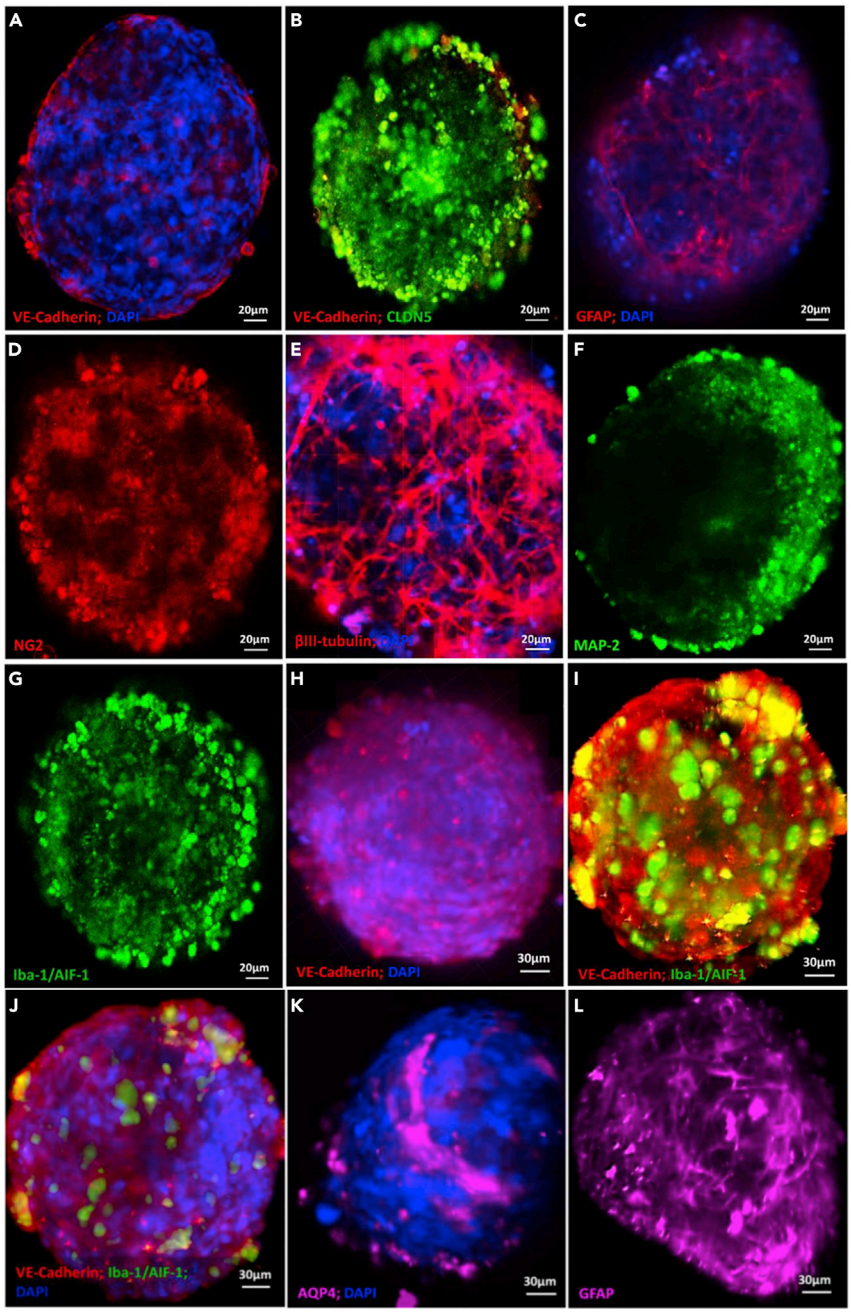

Figure 3. Immunocytochemical characterization of the biofabricated 5-cell spheroids

Representative (A–G) CLSFM and (H–L) LSFM micrographs. Spheroids show the expression of characteristic markers of (A, B, H, I, and J) hCMEC/D3 endothelial cells, (C, K, and L) primary hAs, (D) hBVPs, (E and F) primary rat neuron, and (G, I, and J) primary rat microglia. Cell nuclei in A, C, E, H, J, and K are stained with 4′,6-diamidino-2-phenylindole (DAPI, blue).

3D culture (Balasubramanian et al., 2016; Hawkins et al., 2015; Placone et al., 2015). In line with previous works, we confirmed that hAs cultured in heterocellular spheroids exhibit a ramified phenotype that resembles cortical astrocytic networks, as opposed to 2D cultures where this cell type exhibited enlarged cell bodies, with less and shorter processes (Figure 1C). This phenotype may contribute to regulate the permeability of the BBB, either independently or in concert with other neighboring neuron-glia cells (Banerjee and Bhat, 2007). Furthermore, we performed Western blot analysis and confirmed unequivocally the expression of key proteins such as VE-cadherin (120 kD), β-III tubulin (55 kD), GFAP (52 kD), and

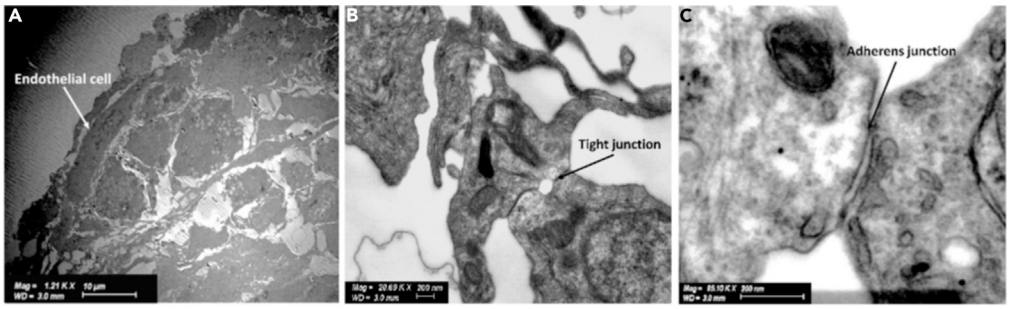

Figure 4. Ultrastructural characterization of hCMEC/D3 endothelial cells in 5-cell spheroids
Representative STEM micrographs showing (A) the organization of hCMEC/D3 endothelial cells on the spheroid surface and the formation of (B) tight junctions and (C) adherens junctions.

Iba-1/AIF-1 (19 kD) (Figure S5A). As detailed above, to fabricate the heterocellular spheroids, cell suspensions of hCMEC/D3, hAs, hBVPs, and primary neurons and microglia cells at a 4:2:1:1:1 cell number ratio were seeded e.g. in non-adherent 96-well plates. This cell number ratio mimics the ratio of these five cell types in the CNS (Zlokovic, 2008) in which microglia comprise 10–15% of the total cell population (Lawson et al., 1992). Weak signals for some of the proteins such as Iba-1/AIF-1 stem from the smaller relative number of some cell types (e.g., microglia) per spheroid with respect to others and the consequent lower relative concentration of the corresponding antigen. It is also worth mentioning that in this electrophoresis analysis, we ran several sodium dodecyl sulfate-polyacrylamide gel electrophoresis (SDS-PAGE) gels, and all of them showed multiple bands for VE-cadherin (Figure S5B). This result was expected because cadherins are transmembrane glycoproteins with several isoforms, as indicated in the Human Protein Atlas (https://www.proteinatlas.org/search/CD144). This also suggests that this protein could undergo recycling inside the complex cell-cell environment and that the fragments detected in this experiment were a result of intracellular protein recycling (Kowalczyk and Nanes, 2012). To ensure that the level of total protein seeding in all the runs was similar, we stained the gels with Coomassie blue staining directly after running gel electrophoresis (data not shown).

While other protocols to produce cortical neuron organoids biofabricated from stem cells would allow the formation of mature neural networks *in situ* (Trujillo et al., 2019), the generation of these structures is usually variable and not reproducible in spheroids made mainly of post-mitotic and already differentiated cells, as in this work. Our focus in this first study was to produce a BBB endothelium that mimics better the *in vivo* phenotype and serves as a platform for the screening of the interaction of the BBB with different NPs. As shown below, RNA-Seq results demonstrated that the culture of BBB endothelial cells in 3D heterocellular spheroids increases the expression of proteins of tight and adherens junctions, which play a fundamental role in controlling the BBB permeability. The investigation of the neuronal differentiation, deep cortical and superficial layer neurons, and the maturation of neuronal networks in spheroids usually requires longer incubation times and it was beyond the scope of this first work. At the same time, some of our 5-cell constructs in a low-serum culture medium exhibited the incipient formation of neuronal networks even after 5 days probably owing to the presence of a small population of neural stem/progenitors in the primary neuronal cultures (Figure 3E).

Cellular organization and ultrastructure

To gain a deeper understanding on the ultrastructure and fundamental homotypic and heterotypic cell-cell interactions in these heterocellular spheroids, we analyzed them by STEM and characterized endothelial, neuronal, glia, and pericyte compartments, the formation of synapses, morphofunctional communication sites between microglial processes, and neuronal cell bodies and the recruitment of phagocytic cells. This technique is advantageous because immunocytochemical staining is not needed. In addition, it can be utilized to visualize the interaction of the different cells with metallic and carbonaceous NPs (see below).

Consistent with our observations by CLSFM and LSFM, hCMEC/D3 endothelial cells are characterized by an elongated shape on the spheroid surface, irregular nuclei, and tightly regulated syncytium of the outer spheroid surface (Figure 4A).

A detailed ultrastructural analysis at the point of cell-cell connections between endothelial cells on the surface of each spheroid revealed the formation of dense strands of tight and adherens junctions (Figures 4B and 4C). The outer endothelial cell-covered spheroid surface (Figures 4A and S2) would recapitulate the phenotype of these cells in the BBB and govern the transport of NPs and other nano-objects (e.g., viruses) into the spheroid and serve as a tool to compare their relative permeability.

The brain comprises billions of neurons that communicate with each other through an intricate web of axons and dendrites. Further ultrastructural studies of 5-cell neuron- and microglia-containing spheroids were conducted by STEM to reveal the presence of subcellular structures and key homotypic and heterotypic cell-cell interactions. Ultrastructural analysis can also shed light into the preservation of the healthy phenotype and of possible toxicity pathways. Primary neurons displayed regular shape and the presence of organelles such as the Golgi apparatus (Figure 5A). Neurons and their stem cells possess a single, non-motile specialized organelle called primary cilium that plays a key role in sensing and responding to the neuronal environment. The primary cilium would act as an "antenna" surveying the extracellular milieu, accepting, and transmitting various signals to the neighboring cells. Structurally, primary cilia lack the central pair of microtubules, which would explain the lack of motility (Lee and Gleeson, 2010). The axoneme contains nine peripheral microtubule doublets, consisting of tubules, lacking the central pair (9 + 0 pattern), as shown in Figure 5B. Putatively, neuroepithelial lining has multiple motile (and not non-motile as in neurons) cilia. Microglia, the resident macrophages of the CNS, do not display primary cilia (Sipos et al., 2018) while mature oligodendrocytes (not included in our 5-cell spheroids) may also have primary cilia (Louvi and Grove, 2011), but no direct evidence has been shown. In addition, ultrastructure cross-sections showed the presence of intracellular structures that are consistent with myelin sheaths that wrap neuronal axons (Figure 5C). Myelin wraps are a specialized membrane produced by oligodendrocytes, and it is composed of a very high dry mass of lipids (70–85%) and a smaller amount of proteins (15–30%), serves as a neuronal insulator, and enables the transmission of electrical impulses between neurons back and forth quickly (Aggarwal et al., 2011).

Our 5-cell spheroids do not comprise oligodendrocytes. However, since neurons along with their stem/progenitors were isolated from rat brains and spheroids were grown in low-serum differentiation medium, the differentiation of oligodendrocyte progenitor cells could explain this observation (Darbinyan et al., 2013; Kerman et al., 2015; Rowitch and Kriegstein, 2010). This analysis provided an experimental proof that microglia, a CNS macrophage, interacts with primary neurons and their synapses (Figure 5D). Furthermore, this technique provided direct ultrastructural evidence that neurons are essential for immune cell-neuron communication (Figure 5D), which is in line with the neuroprotective effect of microglia. Microglial cell bodies can be discerned from other cell types by a smaller size (3–6μm), electron-dense cytoplasm, bean-shaped nuclei, and the accumulation of light inclusions known as lipid bodies (Figures 5D and 5E). They also display a ring of cytoplasm separating the nucleus from the cell membrane, contain few organelles within a single ultrathin section, and a distinct thick, dark band of electron-dense heterochromatin located near the nuclear envelope with pockets of compact heterochromatin nets throughout the nucleus (Figure 5D). Microglia play the role of a dynamic sensor of the brain environment by forming motile processes and by constantly interacting with neighboring neurons, promoting proper neuronal wiring and activity, and protecting them from external insults. Our results confirmed the presence of microglial processes, synaptic vesicles, and morphofunctional microglia-neuronal communications in the spheroids (Figure 5F). Microglia are dynamic cells and surveil their microenvironment in co-culture with primary neurons via glial processes (Video S3A). In addition, they regulate the homeostasis and protect neurons by the phagocytosis of cell debris, contributing to the migration of neural precursor cells (Video S3B). A critical phase in the development of the CNS is cell migration, often over long distances, from their origin to their mature site. Our spheroids displayed neuronal processes that would be consistent with neuronal migration (Figure 5G), an essential stage for the development of the nervous system. As discussed above, the formation of mature neuronal networks is not common in early-stage neocortical 3D cell constructs fabricated with differentiated cells and incubated for short times. However, the presence of a small population of neural stem progenitors in primary neuron cultures could not be ruled out. These progenitor cells together with culture conditions that mimic better the physiology of the CNS would lead to the formation of an incipient neuronal network. Neuronal differentiation and the formation of deep cortical and superficial neuronal layers will be comprehensively investigated in our future work. Astrocytes, like other glial cells, have been commonly presumed as mere support for the function of neurons in the CNS. At the ultrastructural level, astrocytes can be identified by an irregular, stellate shape, with numerous glycogen granules, bundles of intermediate filaments, and a

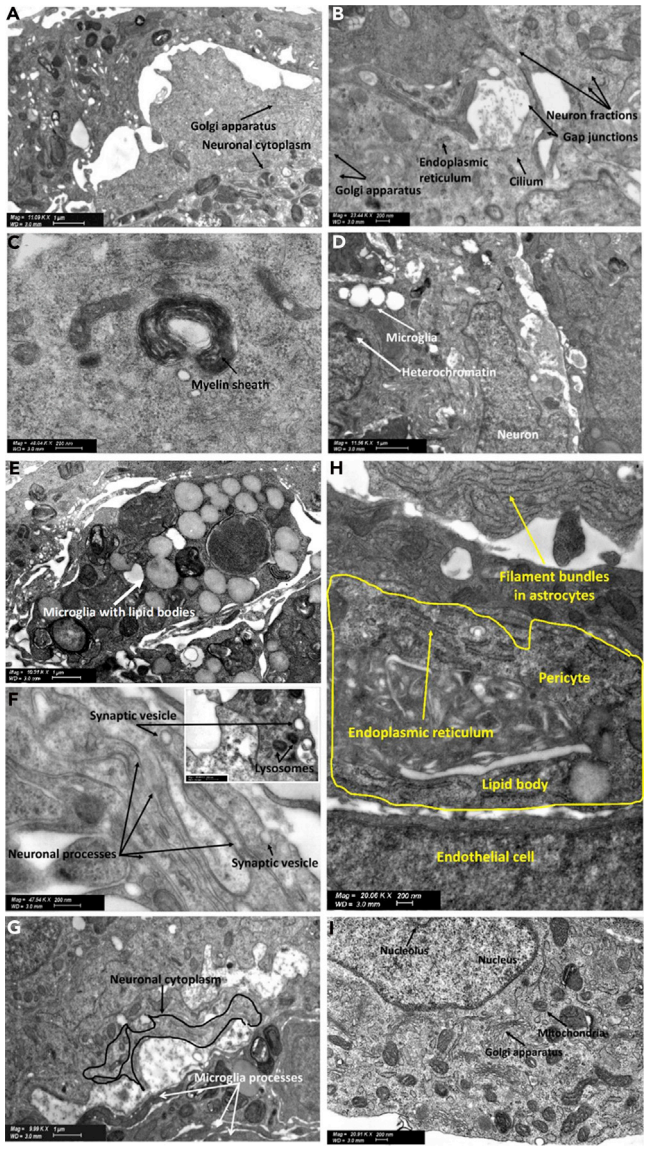

Figure 5. Ultrastructural characterization of neurons and microglia in 5-cell spheroids

Representative STEM micrographs showing (A) part of a neuronal cytoplasm and the presence of Golgi apparatus, (B) neuronal fractions, the primary neural specific cilium lined on the surface of the spheroid, Golgi apparatus, endoplasmic reticulum, and ribosomes, (C) a myelinated sheath in the spheroids along with electron-dense Nissl bodies of the neuronal cytoplasm (indicated with dotted circles), (D) microglia with thicker heterochromatin grains that stand out in the nucleus and the neuronal junctions, (E) lipid bodies characteristic of microglia, (F) neuronal processes and release of synaptic vesicles (black arrow), (G) microglial processes connecting specialized areas of the neuronal cytoplasm, (H) endothelial cell process extending to form a junction with an overlying pericyte, and (I) neuronal cytoplasm containing characteristic features such as the oval-shaped nucleus of a neuron containing the nucleolus, neuronal perikaryal contains multivesicular bodies (small black dots around), mitochondria, and Golgi apparatus.

relatively clear cytoplasm (Figure 5H). STEM studies confirmed the formation of pericyte-endothelial cell connections that have a peg and socket arrangement (Figure 5H) and that enable signal transmission mediated by the release of VE-cadherin (Figures 3A, 3B, 3J, and 3K). The region of the neuronal perikaryon containing the nucleus and nucleolus and that is considered as a metabolic center of the neuronal cell and contains many other functional organelles such as Golgi apparatus, mitochondria due to higher energy consumption could be also observed (Figure 5I).

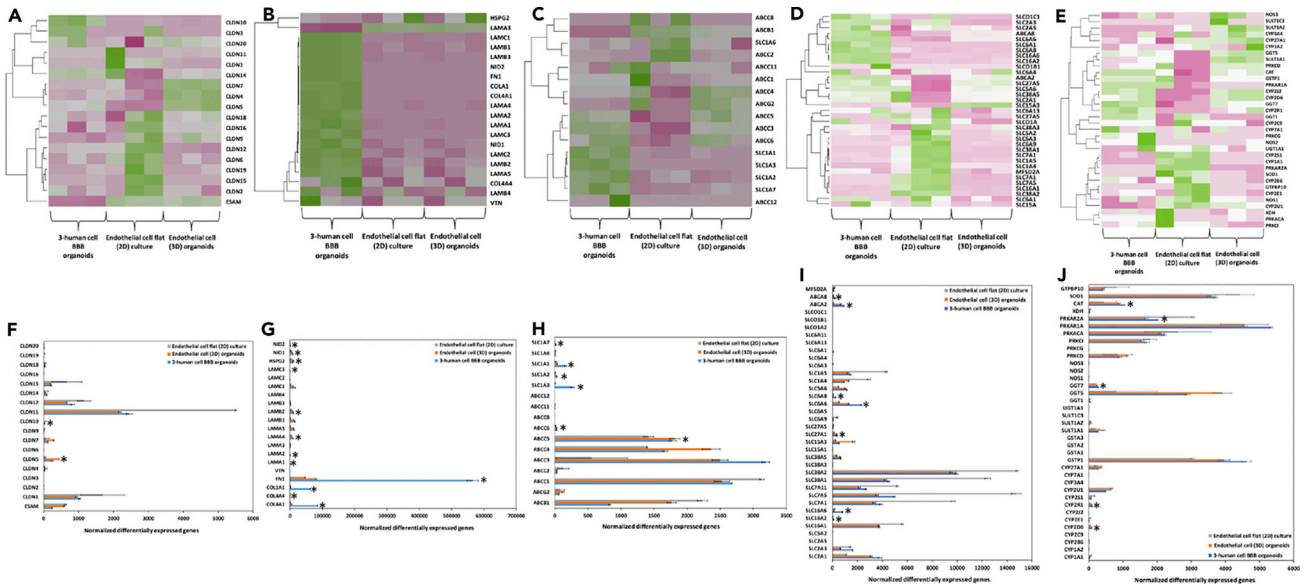

Figure 6. Transcriptomic (RNA-Seq) analysis

Heatmap of RNA-Seq and differentially expressed genes (DEGs) upregulated analysis of 3-human cell spheroids and 2D and 3D endothelial cell monocultures (n = 3 for each culture condition). Green and pink indicate up-regulation and down-regulation, respectively. Average of hierarchical clustering indicates the interclass correlation between all three groups. Selected differential expression of genes encoding for (A and F) tight junction proteins, (B and G) extracellular matrix (ECM) proteins, (C, D, H, and I) ABC efflux transporters, solute carriers (SLCs) and other nutrient transporters, and (E and J) metabolic enzymes. *Significantly differentially expressed genes (DEG) ($p_{adj} < 0.05$, | fold change | >2, base mean ≥ 20). To provide optional filtering criteria in addition to the p_{adj}, additional criteria of |fold change| >2 (|log2 fold change| >1) and average expression level higher than 20 (base Mean > 20) were used.

RNA sequencing

One of the challenges in the production of heterocellular NVU spheroids is to achieve an endothelial cell phenotype that resembles the function *in vivo* because the BBB endothelium regulates the transport of soluble and particulate matter into the CNS. We anticipated that 3D co-culture with hAs and hBVPs would result in a more physiological endothelial cell phenotype.

To analyze whether our heterocellular spheroids exhibit physiological characteristics of the *in vivo* BBB and constitute a functional barrier or not, we evaluated and compared transcriptome expression by RNA-Seq at day 5. Owing to interspecies variabilities and the complexity of analyzing human and rat genes in the same specimens (Breschi et al., 2017), for these studies, we used 3-cell spheroids comprising only hCMEC/D3 cells, hAs and hBVPs (1:1:1 cell number ratio), and compared them to 2D and 3D endothelial cell monocultures; endothelial cell monolayers are the most common *in vitro* model of the BBB (Weksler et al., 2013).

The quality of the extracted RNA was assessed by 1% agarose gel electrophoresis and the quantity and the purity (quality control) of the RNA samples by using the Qubit and TapeStation; all the samples showed RNA integrity values above 8 (Table S1).

To visualize transcriptomic differences between 3-human cell BBB spheroids, endothelial cell (3D) spheroids, and endothelial flat (2D) cultures in genes coding for key structural and functional proteins, a heatmap was generated showing log2 (fold change) >2 (Figures 6A–6E); for each group, three independent biological replicates were analyzed (n = 3).

Based on the criteria given in the experimental section, the number of reads ranged from 21,842,753 to 27,419,486 per sample (Tables S2 and S3). We performed principal components analysis (PCA) on variable groups (excluding the outlier endothelial cell flat culture) to identify genes that are most informative for defining cell subpopulations (Figure S6). PCA plots were useful for visualizing the overall effect of experimental covariates and on each model. The percentage of uniquely mapped reads ranged from

93.87 to 95.28 per sample (Table S4). As a first step to compare the transcriptomic effects on 3-human cell BBB spheroids, endothelial cell (3D) spheroids, and endothelial cell (2D) monolayers, comparative data were generated to display the number of differentially expressed transcripts. To assess whether the transcript was similarly altered in the transcriptomes produced in response to cell-cell interactions including endothelial-astrocyte-pericyte ones in the 3-cell spheroids, a more detailed comparison was carried out by showing a heatmap that represents the quantitative fold change value under each spheroid model (Figures 6A–6E). These initial analyses revealed that heterocellular spheroids and both 2D and 3D endothelial cell monocultures express key genes (Figure 6). To determine whether these gene expression profiles were statistically different between the three groups, we analyzed RNA-Seq data by using the Pearson correlation coefficient and unsupervised hierarchical clustering. According to heatmaps, the gene expression profile of 3-human cell spheroids generally differed from that of 2D and 3D endothelial cell monocultures.

The three groups showed close distance within samples. We assume that there is a different cell milieu and that in the 3-cell spheroids, most transcripts stem from endothelial cells. Next, we confirmed the differentially expressed genes between the three different groups. We set the threshold to $p_{adj} < 0.05$ and FC > 2. Results showed that 7314 genes were up-regulated in 3-cell spheroids with respect to endothelial cell 2D cultures, 3966 genes were up-regulated in 3-cell spheroids with respect to endothelial cell 3D cultures, 6290 genes were up-regulated in endothelial cell 2D cultures with respect to endothelial cell 3D cultures, and 6273 genes were downregulated in 3-cell spheroids with respect to endothelial cell 2D cultures (Table S5). Due to the relevance of tight and gap junction proteins, ECM proteins, SLC influx transporters, ABC efflux transporters, and metabolic enzymes to the barrier function of the BBB endothelium, a more detailed comparison and discussion of the expression of genes coding for these proteins in the three models is included below.

Tight and gap junction proteins

The expression of VE-cadherin and CLDN5 in endothelial cell 2D monocultures and 5-cell spheroids was initially demonstrated by immunocytochemistry (Figures 1 and 3). At this stage, we looked into the expression of genes of the *CLDN* family and *ESAM* that codes for the endothelial cell-specific adhesion molecule (ESAM), a transmembrane junction protein with a similar structure to junctional adhesion molecules (Stamatovic et al., 2016).

Three-cell spheroids overexpressed *CLDN5* which is by far the predominant CLDN in the endothelium that codes for the integral membrane tight junction protein CLDN5 and is a gatekeeper of neurological functions (Figures 6A and 6F) (Günzel and Yu, 2013). The expression of this gene was maximum in 3D endothelial cell monocultures because the number of endothelial cells is greater than that in 3-cell spheroids. *CLDN1* and *CLDN12* were also expressed, though to a lower extent than in endothelial cell 2D monocultures (Figures 6A and 6F); *CLDN12* is not required for BBB tight junction function. In endothelial cell 2D monocultures, the expression of *CLDN* genes was in general lower than that in both 3D systems except for *CLDN1*, *CLDN11*, and *CLDN12* (Figures 6A and 6F). In all the systems, the expression of *CLDN1*, *CLDN2*, *CLDN3*, *CLDN4*, *CLDN6*, *CLDN7*, *CLDN8*, *CLDN9*, *CLDN11*, *CLDN14*, *CLDN16*, *CLDN17*, *CLDN18*, and *CLDN20* transcripts was relatively low (Figures 6A and 6F); these genes are more specific of epithelial (and not endothelial) tight junctions (Garcia-Hernandez et al., 2017; Günzel and Yu, 2013; Seker et al., 2019; Wolburg et al., 2001). A relatively high level of *CLDN15* could be observed in endothelial cell monocultures, while *CLDN19* expression was detected in the 2D endothelial cell model but not in 3D spheroids (Figures 6A and 6B). *ESAM* was also expressed at a lower level in 3-cell spheroids than in endothelial cell 2D monocultures (Figures 6A and 6F) because endothelial cells of mesoderm origin selectively encode the immunoglobulin family adhesion molecule ESAM, which mediates cell-cell adhesion through homophilic molecular interactions (Hirata et al., 2001). Other genes up-regulated in 3-cell spheroids with respect to endothelial cell 2D and 3D monocultures were *GJA1* that codes for the gap junction alpha-1 protein (GJA1) also known as connexin-43 (Table S6) (Zhao et al., 2018). Connexin hemichannels and gap junctions contribute to maintain the physiology of the BBB, participate in paracrine communication, and mediate efficient and rapid bidirectional inter-cellular transmission of electrical and chemical signals. Similarly, we found the upregulation of *VCAM1* that codes for the vascular cell adhesion molecule-1 protein, which mediates endothelial cell adhesion and *VWF* that codes for the von Willebrand factor, a glycoprotein that might be involved in brain homeostasis (Table S6) (Suidan et al., 2013).

Extracellular matrix proteins

The ECM consists of multimeric proteins and proteoglycans that participate in cellular migration and differentiation and function as a support system for endothelial cells and astrocytes, and it is pivotal for development, function, and regulation of vasculature, tight junctions, neurons, and astrocytes through cellular signaling and adhesion (Henrich-Noack et al., 2019; Novak and Kaye, 2000). Lack of any ECM component can result in developmental and functional flaws. Structurally, the BM is a highly organized protein sheet with a thickness of 50–100 nm. Biochemically, the BM consists of four major ECM proteins: collagen type IV, laminin, nidogen, and perlecan (Figure S7). In this context, we analyzed genes coding for key BM proteins.

Collagen type IV is the most abundant component of the BM. The α-chain of this protein consists of three domains, and it is thought that six α-chains self-assemble into triple-helical molecules and form spider web-like scaffolds that interact with laminin (Kalluri, 2003). *COL4A1* and *COL4A4* that code for collagen IV α-chains are upregulated in our 3-human cell spheroids with respect to endothelial cell monocultures (Figures 6B and 6G); COL4A1 is a highly conserved protein across species and is involved in angiogenesis.

Laminin is a T-/cruciform-shaped trimeric protein composed of α, β and γ chains. Brain endothelial cells, pericytes and astrocytes produce different isoforms of laminin at the BBB. *LAMA1*, *LAMA2* and *LAMA4* (coding for laminin α1, α2 and α4, respectively), which regulate the maturation and function of the BBB, and *LAMB2* and *LAMC3* (coding for β and γ chains of laminin) were also upregulated in our heterocellular spheroids (Figures 6B and 6G). Other genes showing higher expression in 3-human cell spheroids than in endothelial cell monocultures were *HSPG2* (coding for perlecan, the core protein of the glycosaminoglycan heparin sulfate) and *NID1* and *NID2* (coding for nidogen-1 and 2, respectively) that serve as linker for collagen IV, laminin and other ECM proteins (Figures 6B and 6G). These results support the formation of a more physiologically relevant BBB endothelial phenotype in the spheroids.

Active efflux transporters

ABC transporters are highly expressed by the BBB endothelium, and they play a key role in maintaining the brain homeostasis because they actively govern the entry of compounds from the bloodstream into the CNS (Kumarasamy and Sosnik, 2020; Qosa et al., 2015). As expected, 3-cell spheroids expressed a moderately higher amount of genes coding for P-glycoprotein (*ABCB1*) and several multidrug resistance proteins (MRPs) of the C subfamily (*ABCC3*, *ABCC4*, *ABCC5*, *ABCC10*, and *ABCC11*) (Figures 6C and 6H); it is noteworthy that endothelial cells represent only ~1/3 of the cells in the heterocellular spheroids. MRP3 is a glycoprotein with a similar molecular mass as MRP2, with similar amino acid composition, and with overlapping substrate specificity. Human MRP3 is the only basolateral efflux pump shown to transport bilirubin glucuronides. In some cases such as *MRP2* (*ABCC2*) deficiency, *MRP3* (*ABCC3*) is strongly upregulated (Figures 6C and 6H). *MRP1* (*ABCC1*), *MRP2* (*ABCC2*), *MRP7* (*ABCC7*), and *MRP8* (*ABCC8*) were not substantially expressed in any of the models (Figures 6C and 6H).

The alanine, serine, and cysteine transporters belong to the SLC1A family of excitatory amino acid transporters (EAATs), Na^+-dependent proteins that reside in the membrane of astrocytes, neurons, and the abluminal (brain-facing) membrane of the BBB (Hawkins and Viña, 2016). EAATs are involved in the efflux transport of glutamate across the BBB and ensure low levels of this neurotransmitter in the interstitial brain fluids.

Genes coding for EAAT1 (SLC1A3, GLAST), EAAT2 (SLC1A2, GLT1), EAAT3 (SLC1A1, EAAC1), and EAAT5 (SLC1A7) proteins were upregulated in 3-cell spheroids with respect to 2D and 3D endothelial cell monocultures (Figures 6D and 6I), most probably due to the contribution of hAs to the total expression. These results were in good agreement with previous works that showed their expression in endothelial cells isolated from brain capillaries (O'Kane et al., 1999).

Active influx transporters

Different influx transporters are involved in the transport of essential endogenous nutrients (e.g., amino acids, glucose) from the bloodstream into the CNS and are critical for the normal function of the brain (Tsuji, 2005). Endothelial cell 3D monocultures expressed relatively high levels of *SLC2A3* (*GLUT3*) encoding for glucose transporter-3 (GLUT3) (Figures 6D and 6I), a pump that is more characteristic of all neurons (Simpson et al., 2008), and did not express *SLC2A5* (*GLUT5*) that codes for the transporter GLUT5

(characteristic of enterocytes) (Douard and Ferraris, 2008). Our 3-cell spheroids expressed high levels of genes coding for different glucose transporters (Figures 6D and 6I). Of special interest is *SLC2A1* (*GLUT1*) that codes for GLUT1 which is crucial for the development of the cerebral microvasculature with BBB features *in vivo* (Zheng et al., 2010). Glucose is the predominant energy source for the brain and heart; for instance, the brain is the most energy-demanding organ in which the endothelium and astrocytes play a major role in regulating their metabolism (Benarroch, 2014). The transport of glucose across the BBB into the brain is mediated by the facilitative GLUT1. This gene was upregulated in the 3-cell spheroids with respect to endothelial cell 3D and 2D monocultures, which constitutes another confirmation of a more physiological phenotype of the endothelium in our heterocellular construct than in endothelial cell monocultures.

Other genes that were overexpressed in 3-cell spheroids when compared to 2D and 3D endothelial cell monocultures are *SLC16A2* (*MCT2*) and *SLC16A6* (*MCT6*) that code for proton-coupled monocarboxylic acid transporters and *SLC6A6* coding for Na^+- and Cl^--dependent taurine transporter (TauT) (Figures 6D and 6I). TauT plays a key role in many pathways such as neurotransmission. *SLC6A1*, the gene coding for the voltage-dependent gamma-aminobutyric acid (GABA) transporter SLC6A1, was also upregulated in the 3-cell spheroids. This transporter is responsible for the re-uptake of GABA from the synapse; GABA counterbalances neuronal excitation in the brain, and any disruption of this balance may result in seizures. A similar trend was observed for *ABCA2* and *ABCA8*, coding for ABCA2, an endo-lysosomal protein that plays an important role in the homeostasis of various lipids and Alzheimer disease, and ABCA8 that regulates the lipid metabolism and is implicated in various CNS pathologies (Kim et al., 2008). *SLC27A1* coding for the long-chain fatty acid transport protein 1 was also overexpressed in the 3-cell models (Figures 6D and 6I).

Metabolic enzymes

Metabolizing enzymes of the BBB have a functional role in the local metabolism of drugs and other xenobiotics (Agúndez et al., 2014). Thus, the overexpression of genes coding for them is an additional proof of the more physiological behavior of an *in vitro* cellular model. Three-cell spheroids expressed high levels of cytochrome P450 genes including *CYP2D6* and *CYP2R1* that were low in 2D and 3D endothelial cell monocultures (Figures 6E and 6J). Conversely, the expression of genes such as *GSTP1*, *SULT1A*, and *UGT1A1* coding for phase-II metabolic enzymes glutathione S-transferase π, sulfotransferase 1A1, and UDP-glucuronosyltransferase, respectively, was low in all the specimens (Figures 6E and 6J). In addition, *SOD1*, a gene coding for the apoptotic enzyme superoxide dismutase 1, and *GTPBP10* for a mitochondrial protein were downregulated in 3-cell spheroids, whereas upregulated in endothelial cell 2D cultures (Figures 6E and 6J). These results indicated that our spheroids do not exhibit hypoxic conditions.

Overall, the comprehensive RNA-Seq analysis of our biofabricated 3-cell spheroids confirmed high relative expression of endothelial cell-specific genes involved in key signaling pathways that contribute to the establishment of a more functional BBB endothelium.

Interaction of nanoparticles with 5-cell spheroids

Our previous investigations conducted with primary rat cells suggested that neither forebrain nor olfactory neurons internalize polymeric NPs (Kumarasamy and Sosnik, 2019) and that, without the surface modification with a peptide shuttle, some of them cross the BBB *in vitro* and *in vivo* to a limited extent (Bukchin et al., 2020, 2021). Conversely, they were internalized by primary microglia *in vitro* (Kumarasamy and Sosnik, 2019). These studies were conducted in 2D monocultures. Homotypic and heterotypic cell-cell connections between different components of the CNS, including neurons and microglia, in 3D may contribute to generate a more physiological milieu to increase the integrity and the function of the BBB endothelium and reciprocally affect the phenotype of the other cells actively implicated in the interaction with particulate matter such as microglia (Watson et al., 2017).

The transport of nanomaterials across the BBB endothelium is usually by transcytosis due to the presence of tight and adherens junctions, and it is initiated by endocytosis, for which the size should be $\leq$ 200 nm (Ceña and Játiva, 2018; Nowak et al., 2020). Depending on the shape and surface properties, particles as large at 500 nm could be transported to some extent (Nowak et al., 2020). As explained above, a major limitation of the existing *in vitro* models is that usually they do not include CNS macrophages. Upon comprehensive characterization of our heterocellular spheroids and confirmation that BBB endothelial cells cultured in

these constructs form an almost complete monolayer on the spheroid surface and express higher amounts of key tight, adherens and gap junction proteins than endothelial cell monocultures, we studied the ability of different polymeric, ceramic, and metallic NPs to cross this outer endothelial cell monolayer and reach the spheroid bulk.

In a previous work, we demonstrated that the permeability of fluorescently labeled dextran (average molecular weight of 40,000 g/mol, 0.001% w/v), a probe used to estimate the tightness of the BBB endothelium *in vitro*, is in the same range measured for other dextrans (Bukchin et al., 2020, 2021). Based on immunostaining and RNA-Seq data, we anticipated that BBB endothelial cells cultured in 5-cell spheroids display even lower permeability than those in 2D monoculture systems. The properties of the NPs used in this work are summarized in Table S7. Before use, NPs were diluted under sterile conditions and mixed with the corresponding culture medium to the final desired concentration.

Polymeric nanoparticles

In this work, we used four amphiphilic polymeric NPs produced by the self-assembly of chitosan (CS)- (Noi et al., 2018; Schlachet and Sosnik, 2019; Schlachet et al., 2019), poly(vinyl alcohol) (PVA)- (Moshe Halamish et al., 2019), and hydrolyzed galactomannan (hGM)-based graft copolymers (Zaritski et al., 2019) synthesized by the free radical graft polymerization of methyl methacrylate onto the polymer backbone and the formation of poly(methyl methacrylate) (PMMA) pendant blocks (Table S7). NPs displayed sizes between 92 $\pm$ 4 and 463 $\pm$ 73 nm and from positive to negative Z-potential; these two properties govern the interaction of nanoparticulate matter with cells (Mailänder and Landfester, 2009) and were measured immediately before the biological experiments. It is worth stressing that these NPs showed good cell compatibility with a broad spectrum of cell types *in vitro*, including epithelial and endothelial cells (Moshe Halamish et al., 2019; Kumarasamy and Sosnik, 2019; Noi et al., 2018; Schlachet and Sosnik, 2019; Schlachet et al., 2019; Zaritski et al., 2019), as measured by metabolic and morphological assays.

We hypothesized that owing to the cellular heterogeneity of the 5-cell spheroids, some immunocompetent cells (e.g., microglia) could be more susceptible to damage or, conversely, to uptake the NPs to a greater extent than others (e.g., neurons) (Kumarasamy and Sosnik, 2019). Primary rat microglia cells cultured in 2D and exposed to the different polymeric NPs used in this work remained viable and did not exhibit morphological changes (Kumarasamy and Sosnik, 2019). However, the behavior of microglia in 3D heterocellular systems has not been investigated before.

To address these questions, polymeric NPs were fluorescently labeled by conjugation of fluorescein isothiocyanate (FITC, green fluorescence) or rhodamine isothiocyanate (RITC, red fluorescence) to the backbone of the graft copolymer before preparation and their interaction (e.g., permeability) with 5-cell spheroids after 24 hr of exposure characterized by CLSFM and LSFM. In general, studies revealed that 0.1% w/v NPs do not cause any morphological damage to the spheroids and that the cell density is preserved (Figure 7). When 5-cell spheroids were exposed to cross-linked mixed CS-PMMA30:PVA-PMMA17 NPs, most of them accumulated on the spheroid surface and only a small fraction could be found inside it, as shown in Figures 7A and 7B by 2D and 2.5D CLSFM. However, cross-sectional CLSFM images cannot provide complete multi-view volumetric information of 3D spheroids for which we need to detect the fluorescence intensity of each individual voxel. Thus, cell uptake was also investigated by LSFM. Images taken from different angles confirmed that, as opposed to CLSFM, some NPs permeate into the spheroids and suggested the possible involvement of astroglia or microglia in the transport of CS-PMMA30:PVA-PMMA17 NPs (Figures 7C and 7D; Video S4A). In case of mild injury/disturbance, astrocytes become phagocytes which remove "foreign" material and produce anti-inflammatory cytokines. Conversely, under excessive injury/insult, "reactive" astrocytes produce proinflammatory cytokines that recruit and activate microglia (Greenhalgh et al., 2020; Jha et al., 2019). Both pathways could be involved in the uptake of the NPs into the spheroid bulk. These findings are in good agreement with previous *in vivo* studies that showed the limited bioavailability of this kind of NPs in the brain of mouse after intravenous injection (Bukchin et al., 2020; Schlachet et al., 2020). Similar results were observed with CS-PMMA33 (Figures 7E–7H, Video S4B), cross-linked PVA-PMMA17 (Figures 7I–7L, Video S4C), and hGM-PMMA28 NPs (Figures 7M–7P, Video S4D). Furthermore, representation of the cells as dots (Figures 7D, 7H, 7L, and 7P) confirmed that these NPs are not harmful to cells and that the cell density was not majorly affected upon a 24 h exposure.

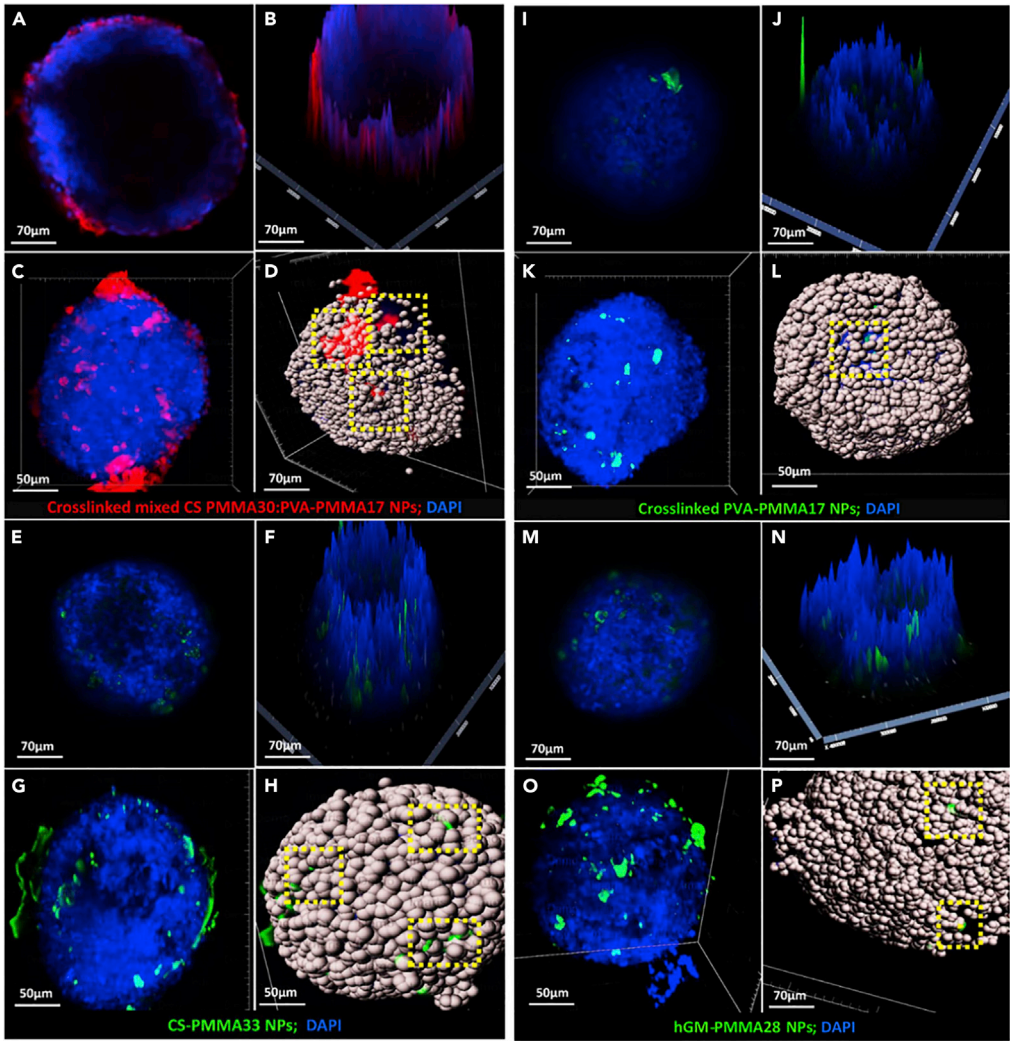

Figure 7. Characterization of the interaction of polymeric nanoparticles with biofabricated 5-cell spheroids

CLSFM micrographs of spheroids exposed to (A and B) cross-linked mixed CS-PMMA30:PVA-PMMA17, (E and F) cross-linked PVA-PMMA17, (I and J) CS-PMMA33, (M and N) hGM-PMMA28 nanoparticles. LSFM micrographs of spheroids exposed to (C and D) cross-linked CS-PMMA30:PVA-PMMA17, (G and H) cross-linked PVA-PMMA17, (K and L) CS-PMMA33, (O and P) hGM-PMMA28 nanoparticles. Cell spots in D, H, and L, and P are included to ease the visualization of the cells and exactly to locate the fluorescent nanoparticles underneath the spheroid surface. Up-taken nanoparticles are highlighted by dotted yellow squares.

Both CLSFM and LSFM analyses strongly suggest that the enhanced fluorescence of NP-exposed spheroids stems from NPs that most probably accumulated within primary microglia or immunocompetent astrocytes. Permeability studies conducted with our 5-cells spheroids and metallic and carbon NPs by STEM further contributed to our understanding of the possible uptake pathways and the intracellular trafficking of the NPs (see below).

The brain is rich in energy-demanding nerve cells that metabolize glucose as the main fuel (Mergenthaler et al., 2013). Neurons consume glucose through glia cells, in which this nutrient is metabolized into lactate by the glycolytic pathway, and transferred to axons and neuronal bodies when needed. To this end and to support their sentinel activity in the CNS, primary microglia overexpress GLUT1 (Wang et al., 2019). In a previous work, we demonstrated that the accumulation of hGM-PMMA28 NPs in pediatric sarcomas *in vivo* correlates well with the overexpression of GLUT1 (Zaritski et al., 2019). Our LSFM results would suggest that these inherently mannosylated nanoparticles are actively transported into the spheroid, most probably by

activated microglia and astrocytes. hGM-PMMA28 and other carbohydrate-based NPs investigated in this work such as cross-linked mixed CS-PMMA30:PVA-PMMA17 and CS-PMMA33 could be also taken up through the mannose receptor that is expressed in microglia and astrocytes and that displays a carbohydrate recognition domain. Boric-acid cross-linked PVA-PMMA17 NPs exhibit a boronated surface that may form complexes with microglia by toll-like receptor 4-myeloid differentiation protein-2 signaling pathway that is activated in inflammation (Hunt and Idso, 1999). In addition, microglia express sialic acid which may also bind boronated NPs (Pappin et al., 2012). These findings are in good agreement with the active surveillance and homeostasis roles of microglia in the CNS microenvironment. Together with the gene expression pattern observed for endothelial cells cultured in 3-cell spheroids with respect to 2D and 3D monocultures, this 5-cell construct would recapitulate better the physiology of the BBB and serve as a platform to assess the interaction of nanomedicines and nano-pollutants with the CNS.

Studies of the co-localization of polymeric NPs and microglia in our 5-cell spheroids were not successful. In our previous work, we found out that nanoparticulate matter reaching the CNS is found only within microglia cells (Murali et al., 2015). Moreover, we confirmed that primary olfactory sensory neurons and cortical neurons isolated from the CNS of rodents do not internalize these polymeric NPs, regardless of their composition, size, and surface charge (Izak-Nau et al., 2014; Kumarasamy and Sosnik, 2019; Murali et al., 2015). These findings, together with other reports (Almalik et al., 2017; Giljohann et al., 2007; Sarmento et al., 2011) in which NPs are taken up by microglia to a higher extent than neurons in 2D culture, represent robust evidence to associate the uptake of the NPs used in this study with the presence of microglia in our 5-cell spheroids. The key role of microglia in NP uptake is also supported by the results obtained with silver, gold, and carbonaceous NPs in which we clearly show their co-localization in the cell cytosol with lipid droplets that are characteristic of microglia by using STEM (see below).

Metallic nanoparticles. The use of metallic NPs in nanomedicine is broad and varied (Singh, 2018). For example, Au and Ag NPs have been proposed in anti-cancer therapy (Chugh et al., 2018), and, upon injection, they could cross the BBB from the systemic circulation and reach the CNS (Dabrowska-Bouta et al., 2018; Rodriguez-Izquierdo et al., 2020; Sela et al., 2015; Tang et al., 2010; Zhou et al., 2018). Several studies used Au NPs as shuttles and demonstrated that the smaller the size, the higher the permeability. For example, 10–20 nm Au NPs resulted in the highest cellular distribution in the brain of mouse (Betzer et al., 2017; Kang et al., 2019). A main drawback of Au NPs is the limited ability of the CNS to eliminate them and the potential neurotoxicity associated with their chronic accumulation.

To assess the performance of our construct, we exposed 5-cell spheroids (5 days old) to Au NPs (10 ± 2 nm, concentration of 1×10^6 NPs/mL, Table S7) for 24 h and analyzed their possible endocytosis by STEM. After 24 h, Au NPs crossed the BBB endothelium (Setyawati et al., 2017) formed on the spheroid surface and were readily taken up and distributed in the cytosol and inside endosomes and lysosomes of primary microglia that were identified by the presence of multiple lipid droplets in the cytosol (Figures 8A and 8B). The uptake mechanism is most probably energy dependent (Hutter et al., 2010). The ultrastructural morphology of microglia phenotype and the high accumulation of lipid bodies are associated with an activated phenotype in which microglia monitor the surrounding environment and endocytose nanoparticulate matter.

Ag NPs have been also used in nanotherapeutics. Ag NPs (60 ± 13 nm, concentration of 1×10^6 NPs/mL, Table S7) were produced by a chemical method, and 5-cell spheroids were exposed to them for the same time. STEM studies focused on intracellular vesicles revealed the presence of only very few Ag NPs within microglia (Figures 8C–8E); note the co-localization of the NPs and lipid droplets. This result would be in line with the more limited ability of these larger NPs (when compared to the smaller Au counterparts) to cross the BBB endothelium formed on the surface of the spheroids. Another possible explanation is that they undergo relatively fast dissolution outside and inside the cells (Jiang et al., 2015; Smith et al., 2018). These findings were consistent along different experiments.

Graphene nanoplates and carbon dots

Among carbon nanomaterials, graphene-based ones are the most popular in the area of nanoneuroscience (Kitko and Zhang, 2019) due to their various applications in neuronanotechnology (Fabbro et al., 2016; Kitko and Zhang, 2019; Pampaloni et al., 2018) and in nanosafety studies (Fadeel et al., 2018; Kim et al., 2018). Here, we investigated the effect of graphene nanoplates (5 μm diameter and 10 nm thickness;

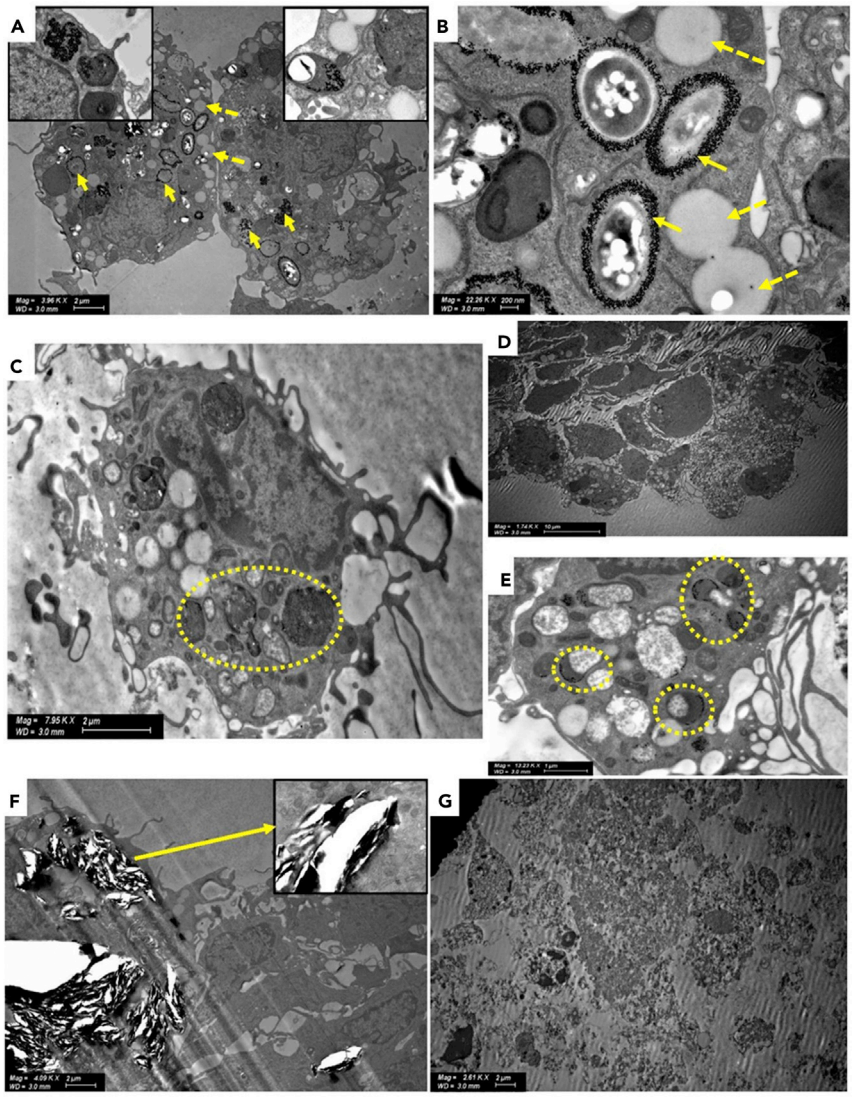

Figure 8. STEM micrographs of 5-cell spheroids exposed to different metallic and carbonaceous nanoparticles

(A and B) Au NPs inside microglia (indicated with yellow arrows) and surrounding endosomes and lysosomes. Cells display characteristic lipid droplets (indicated with yellow dotted arrows).

(C) Ag NPs inside vesicles (indicated with yellow dotted circle) of microglia displaying characteristic lipid droplets.

(D and E) (D) Ag NPs inside microglia clusters, (E) Ag NPs inside endosomes and lysosomes of glia (indicated with yellow dotted circle).

(F) Cell disruption effect of graphene nanoplates on astrocytes (indicated with a yellow arrow in the insert).

(G) Cell destructive effect of alkaline carbon dots on a 5-cell spheroid.

25 μg/mL, Table S7) on our 5-cell spheroids. After 24 h, significant cell death and a sharp decrease in cell density could be observed, most probably due to direct cell damage (Figure 8F). Similarly, alkaline carbon dots (10 nm; 25 μg/mL, Table S7) caused complete destruction of cellular structures (Figure 8G). These results represent another proof of the good cell compatibility of the polymeric NPs investigated in this work.

In recent years, carbon dots have become a rising environmental concern because of their extensive use in energy applications, massive emissions to the air, and likely transport from the nasal mucosa into the CNS. Our results strongly suggest the possible toxicity of these NPs and the need for more systematic investigations that screen their detrimental effect on the CNS upon acute and chronic exposure.

The interplay between other CNS-tissue-type cells, microglia, and different nanomaterials by molecular-level analysis which can provide sufficient sensibility to analyze the functional/phenogenotypic response of this brain's own macrophage cell population (Matcovitch-Natan et al., 2016) was beyond the scope of the present work. In future research, this model will be characterized in other molecular-level and individual cell-specific aspects and will assess the effect of different NPs on the phenotype of primary microglia cultured in heterocellular constructs.

Conclusions

In this work, we biofabricated a 5-cell heterocellular spheroid that combines human endothelial cells, pericytes, and astrocytes with primary neurons and microglia isolated from rat brains in a ratio that mimics the cell composition of the brain tissue. After a comprehensive characterization, we utilized them to study the toxicity and permeability of different types of NPs. Polymeric NPs showed good cell compatibility and underwent uptake to some extent. Similar results were observed with metallic NPs, though the permeability depended on their size. Conversely, carbonaceous NPs were very toxic. The proposed construct is easily biofabricated and scalable. Furthermore, its screening throughput capacity could be increased by integrating automated microscopy and robotics technologies. Overall results confirm that these spheroids are a valuable tool in nanotherapeutics, nanoneurosafety, nanoneurotoxicity, and neuropathology. In the future, the use of all human-derived cells to biofabricate this kind of heterocellular spheroid will improve the clinical predictive value of this platform.

Limitations of the study

Even though we have demonstrated that the heterocellular spheroids express structural and functional proteins of the NV-BBB, the use of rodent immune cells together with human cells may limit the clinical significance of screening studies. In the future, the use of all human-derived cells to biofabricate the heterocellular spheroid will improve the predictive value of this platform.

Resource availability

Lead contact

Further information and requests for resources (e.g., RNA quality and RNA-Seq) and other data should be directed to and will be fulfilled by the lead contact, Prof. Alejandro Sosnik (sosnik@technion.ac.il).

Material availability

This study did not generate any new reagent or material.

Data and code availability

The original unprocessed data and RNA-Seq data sets are available upon request to the corresponding author.

METHODS

All methods can be found in the accompanying Transparent Methods supplemental file.

SUPPLEMENTAL INFORMATION

Supplemental Information can be found online at https://doi.org/10.1016/j.isci.2021.102183.

ACKNOWLEDGMENTS

This work was supported by grants from the Teva National Network of Excellence (NNE) in Neuroscience Research (TEVA NNE) from the Teva Pharmaceutical Industries. This work was partially funded by the Russell Berrie Nanotechnology Institute (Technion-Israel Institute of Technology). The postdoctoral fellowship of MK was funded by the Council for Higher Education of Israel through "The PBC Fellowship Program for Outstanding Chinese and Indian Post-Doctoral Fellows". We thank Nitsan Dahan and Yael Lupu-Haber from the Microscopy Unit at the Technion's Life Sciences & Engineering (LS&E) Interdisciplinary Research Center for kindly providing microscopy image processing support. We also thank Emeritus Prof. Emilia Madarasz from the Hungarian Academy of Sciences for fruitful discussions. We are grateful to the Technion Genome Center (TGC) for their support on RNA sequencing, quality control, and differential expression analyses.

AUTHOR CONTRIBUTIONS

M.K. and A.S. conceptualized and planned the work. M.K. conducted the experiments. M.K. and A.S. analyzed the data. A.S. supervised the work and obtained the funding. The original and revised versions of the manuscript were written by M.K. and A.S.

DECLARATION OF INTERESTS

The authors declare no competing interests.

Received: September 2, 2020
Revised: January 3, 2021
Accepted: February 9, 2021
Published: March 19, 2021

REFERENCES

Abbott, N.J. (2013). Blood-brain barrier structure and function and the challenges for CNS drug delivery. J. Inherit. Metab. Dis. *36*, 437–449.

Aggarwal, S., Yurlova, L., and Simons, M. (2011). Central nervous system myelin: structure, synthesis and assembly. Trends Cell Biol. *21*, 585–593.

Agúndez, J.A.G., Jiménez-Jiménez, F.J., Alonso-Navarro, H., and García-Martín, E.P. (2014). Drug and xenobiotic biotransformation in the blood brain barrier: a neglected issue. Front. Cell. Neurosci. *8*, 335.

Albert-Smet, I., Marcos-Vidal, A., Vaquero, J.J., Desco, M., Muñoz-Barrutia, A., and Ripoll, J. (2019). Applications of light-sheet microscopy in microdevices. Front. Neuroanat. *13*, 1.

Almalik, A., Benabdelkamel, H., Masood, A., Alanazi, I.O., Alradwan, I., Majrashi, M.A., Alfadda, A.A., Alghamdi, W.M., Alrabiah, H., Tirelli, N., et al. (2017). Hyaluronic acid coated chitosan nanoparticles reduced the immunogenicity of the formed protein corona. Sci. Rep. *7*, 10542.

Amin, N.D., and Paşca, S.P. (2018). Building models of brain disorders with three-dimensional organoids. Neuron *100*, 389–405.

Balasubramanian, S., Packard, J.A., Leach, J.B., and Powell, E.M. (2016). Three-dimensional environment sustains morphological heterogeneity and promotes phenotypic progression during astrocyte development. Tissue Eng. A *22*, 885–898.

Banerjee, S., and Bhat, M.A. (2007). Neuron-glial interactions in blood-brain barrier formation. Annu. Rev. Neurosci. *30*, 235–258.

Benarroch, E.E. (2014). Brain glucose transporters: Implications for neurologic disease. Neurology *82*, 1374–1379.

Bergmann, S., Lawler, S.E., Qu, Y., Fadzen, C.M., Wolfe, J.M., Regan, M.S., Pentelute, B.L., Agar, N.Y.R., and Cho, C.F. (2018). Blood-brain-barrier organoids for investigating the permeability of CNS therapeutics. Nat. Protoc. *13*, 2827–2843.

Betzer, O., Shilo, M., Opochinsky, R., Barnoy, E., Motiei, M., Okun, E., Yadid, G., and Popovtzer, R. (2017). The effect of nanoparticle size on the ability to cross the blood-brain barrier: an in vivo study. Nanomedicine (London) *12*, 1533–1546.

Bhalerao, A., Sivandzade, F., Archie, S.R., Chowdhury, E.A., Noorani, B., and Cucullo, L. (2020). In vitro modeling of the neurovascular unit: advances in the field. Fluids Barriers CNS *17*, 22.

Biemans, E., Jäkel, L., de Waal, R.M.W., Kuiperij, H.B., and Verbeek, M.M. (2017). Limitations of the hCMEC/D3 cell line as a model for Aβ clearance by the human blood-brain barrier. J. Neurosci. Res. *95*, 1513–1522.

Breschi, A., Gingeras, T.R., and Guigó, R. (2017). Comparative transcriptomics in human and mouse. Nat. Rev. Genet. *18*, 425–440.

Bukchin, A., Sanchez-Navarro, M., Carrera, A., Teixidó, M., Carcaboso, A.M., Giralt, E., and Sosnik, A. (2020). Amphiphilic polymeric nanoparticles modified with a retro-enantio peptide shuttle target the brain of mice. Chem. Mater. *32*, 7679–7693.

Bukchin, A., Sanchez-Navarro, M., Carrera, A., Resa-Pares, C., Castillo-Hecija, H., Balaguer-Lluna, L., Teixidó, M., Olaciregui, N.G., Giralt, E., Carcaboso, A.M., and Sosnik, A. (2021). Amphiphilic polymeric nanoparticles modified with a protease-resistant peptide shuttle for the delivery of SN-38 in diffuse intrinsic pontine glioma. ACS Appl. Nano Mater. https://doi.org/10.1021/acsanm.0c02888.

Ceña, V., and Játiva, P. (2018). Nanoparticle crossing of blood-brain barrier: a road to new therapeutic approaches to central nervous system diseases. Nanomedicine (London) *13*, 1513–1516.

Cheng, Q., Yang, Y., and Gao, J. (2020). Infectivity of human coronavirus in the brain. EBioMedicine *56*, 102799.

Cho, C.-F., Wolfe, J.M., Fadzen, C.M., Calligaris, D., Hornburg, K., Chiocca, E.A., Agar, N.Y.R., Pentelute, B.L., and Lawler, S.E. (2017). Blood-brain-barrier spheroids as an in vitro screening platform for brain-penetrating agents. Nat. Commun. *8*, 15623.

Chugh, H., Sood, D., Chandra, I., Tomar, V., Dhawan, G., and Chandra, R. (2018). Role of gold and silver nanoparticles in cancer nano-medicine. Artif. Cell Nanomedicine Biotechnol. *46*, 1210–1220.

Cullen, D.K., Gordián-Vélez, W.J., Struzyna, L.A., Jgamadze, D., Lim, J., Wofford, K.L., Browne, K.D., and Chen, H.I. (2019). Bundled three-dimensional human axon tracts derived from brain organoids. iScience *21*, 57–67.

Dabrowska-Bouta, B., Sulkowski, G., Frontczak-Baniewicz, M., Skalska, J., Salek, M., Orzelska-Gorka, J., and Struzynska, L. (2018). Ultrastructural and biochemical features of cerebral microvessels of adult rat subjected to a low dose of silver nanoparticles. Toxicology *408*, 31–38.

Darbinyan, A., Kaminski, R., White, M.K., Darbinian, N., and Khalili, K. (2013). Isolation and propagation of primary human and rodent embryonic neural progenitor cells and cortical neurons. Methods Mol. Biol. *1078*, 45–54.

Das, A., Kim, S.H., Arifuzzaman, S., Yoon, T., Chai, J.C., Lee, Y.S., Park, K.S., Jung, K.H., and Chai, Y.G. (2016). Transcriptome sequencing reveals that LPS-triggered transcriptional responses in established microglia BV2 cell lines are poorly representative of primary microglia. J. Neuroinflammation *13*, 182.

Dawson, T.M., Golde, T.E., and Lagier-Tourenne, C. (2018). Animal models of neurodegenerative diseases. Nat. Neurosci. *21*, 1370–1379.

DiMasi, J.A., Feldman, L., Seckler, A., and Wilson, A. (2010). Trends in risks associated with new drug development: success rates for investigational drugs. Clin. Pharmacol. Ther. *87*, 272–277.

Douard, V., and Ferraris, R.P. (2008). Regulation of the fructose transporter GLUT5 in health and disease. Am. J. Physiol. Endocrinol. Metab. *295*, E227–E237.

Esch, E.W., Bahinski, A., and Huh, D. (2015). Organs-on-chips at the frontiers of drug discovery. Nat. Rev. Drug Discov. *14*, 248–260.

Fabbro, A., Scaini, D., León, V., Vázquez, E., Cellot, G., Privitera, G., Lombardi, L., Torrisi, F., Tomarchio, F., Bonaccorso, F., et al. (2016). Graphene-based interfaces do not alter target nerve cells. ACS Nano *10*, 615–623.

Fadeel, B. (2019). The right stuff: on the future of nanotoxicology. Front. Toxicol. *1*, 1.

Fadeel, B., Bussy, C., Merino, S., Vázquez, E., Flahaut, E., Mouchet, F., Evariste, L., Gauthier, L., Koivisto, A.J., Vogel, U., et al. (2018). Safety

assessment of graphene-based materials: focus on human health and the environment. ACS Nano *12*, 10582–10620.

Feng, X., Chen, A., Zhang, Y., Wang, J., Shao, L., and Wei, L. (2015). Central nervous system toxicity of metallic nanoparticles. Int. J. Nanomedicine *10*, 4321–4340.

Fujii, M., and Sato, T. (2021). Somatic cell-derived organoids as prototypes of human epithelial tissues and diseases. Nat. Mater. *20*, 156–169.

Furtado, D., Bjornmalm, M., Ayton, S., Bush, A.I., Kempe, K., and Caruso, F. (2018). Overcoming the blood-brain barrier: the role of nanomaterials in treating neurological diseases. Adv. Mater. *30*, e1801362.

Garcia-Hernandez, V., Quiros, M., and Nusrat, A. (2017). Intestinal epithelial claudins: expression and regulation in homeostasis and inflammation. Ann. N. Y. Acad. Sci. *1397*, 66–79.

Gibbs, R.A., Weinstock, G.M., Metzker, M.L., Muzny, D.M., Sodergren, E.J., Scherer, S., Scott, G., Steffen, D., Worley, K.C., Burch, P.E., et al. (2004). Genome sequence of the Brown Norway rat yields insights into mammalian evolution. Nature *428*, 493–521.

Giljohann, D.A., Seferos, D.S., Patel, P.C., Millstone, J.E., Rosi, N.L., and Mirkin, C.A. (2007). Oligonucleotide loading determines cellular uptake of DNA-modified gold nanoparticles. Nano Lett. *7*, 3818–3821.

Greenhalgh, A.D., David, S., and Bennett, F.C. (2020). Immune cell regulation of glia during CNS injury and disease. Nat. Rev. Neurosci. *21*, 139–152.

Group, G.B.D.N.D.C. (2017). Global, regional, and national burden of neurological disorders during 1990-2015: a systematic analysis for the Global Burden of Disease Study 2015. Lancet Neurol. *16*, 877–897.

Günzel, D., and Yu, A.S.L. (2013). Claudins and the modulation of tight junction permeability. Physiol. Rev. *93*, 525–569.

Hanes, J., Zilka, N., Bartkova, M., Caletkova, M., Dobrota, D., and Novak, M. (2009). Rat tau proteome consists of six tau isoforms: implication for animal models of human tauopathies. J. Neurochem. *108*, 1167–1176.

Hawkins, R.A., and Viña, J.R. (2016). How glutamate is managed by the blood-brain barrier. Biology (Basel) *5*, 37.

Hawkins, B.T., Grego, S., and Sellgren, K.L. (2015). Three-dimensional culture conditions differentially affect astrocyte modulation of brain endothelial barrier function in response to transforming growth factor beta1. Brain Res. *1608*, 167–176.

Heide, M., Huttner, W.B., and Mora-Bermudez, F. (2018). Brain organoids as models to study human neocortex development and evolution. Curr. Opin. Cell Biol. *55*, 8–16.

Henrich-Noack, P., Nikitovic, D., Neagu, M., Docea, A.O., Engin, A.B., Gelperina, S., Shtilman, M., Mitsias, P., Tzanakakis, G., Gozes, I., et al. (2019). The blood–brain barrier and beyond: nano-based neuropharmacology and the role of extracellular matrix. Nanomedicine: Nanotechnology, Biol. Med. *17*, 359–379.

Hirata, K., Ishida, T., Penta, K., Rezaee, M., Yang, E., Wohlgemuth, J., and Quertermous, T. (2001). Cloning of an immunoglobulin family adhesion molecule selectively expressed by endothelial cells. J. Biol. Chem. *276*, 16223–16231.

Hubbard, J.A., Hsu, M.S., Seldin, M.M., and Binder, D.K. (2015). Expression of the astrocyte water channel aquaporin-4 in the mouse brain. ASN Neuro *7*, https://doi.org/10.1177/1759091415605486.

Hunt, C.D., and Idso, J.P. (1999). Dietary boron as a physiological regulator of the normal inflammatory response: a review and current research progress. J. Trace Elem. Exp. Med. *12*, 221–233.

Hutter, E., Boridy, S., Labrecque, S., Lalancette-Hébert, M., Kriz, J., Winnik, F.M., and Maysinger, D. (2010). Microglial response to gold nanoparticles. ACS Nano *4*, 2595–2606.

Izak-Nau, E., Kenesei, K., Murali, K., Voetz, M., Eiden, S., Puntes, V.F., Duschl, A., and Madarasz, E. (2014). Interaction of differently functionalized fluorescent silica nanoparticles with neural stem- and tissue-type cells. Nanotoxicology *8* (*Suppl 1*), 138–148.

Jha, M.K., Jo, M., Kim, J.H., and Suk, K. (2019). Microglia-astrocyte crosstalk: an intimate molecular conversation. The Neuroscientist *25*, 227–240.

Jiang, X., Miclăuş, T., Wang, L., Foldbjerg, R., Sutherland, D.S., Autrup, H., Chen, C., and Beer, C. (2015). Fast intracellular dissolution and persistent cellular uptake of silver nanoparticles in CHO-K1 cells: implication for cytotoxicity. Nanotoxicology *9*, 181–189.

Kaji, R. (2019). Global burden of neurological diseases highlights stroke. Nat. Rev. Neurol. *15*, 371–372.

Kalluri, R. (2003). Basement membranes: structure, assembly and role in tumour angiogenesis. Nat. Rev. Cancer *3*, 422–433.

Kang, J.H., Cho, J., and Ko, Y.T. (2019). Investigation on the effect of nanoparticle size on the blood-brain tumour barrier permeability by in situ perfusion via internal carotid artery in mice. J. Drug Target. *27*, 103–110.

Kerman, B.E., Kim, H.J., Padmanabhan, K., Mei, A., Georges, S., Joens, M.S., Fitzpatrick, J.A., Jappelli, R., Chandross, K.J., August, P., et al. (2015). In vitro myelin formation using embryonic stem cells. Development *142*, 2213–2225.

Kim, W.S., Weickert, C.S., and Garner, B. (2008). Role of ATP-binding cassette transporters in brain lipid transport and neurological disease. J. Neurochem. *104*, 1145–1166.

Kim, Y.H., Jo, M.S., Kim, J.K., Shin, J.H., Baek, J.E., Park, H.S., An, H.J., Lee, J.S., Kim, B.W., Kim, H.P., et al. (2018). Short-term inhalation study of graphene oxide nanoplates. Nanotoxicology *12*, 224–238.

Kitko, K.E., and Zhang, Q. (2019). Graphene-based nanomaterials: from production to integration with modern tools in neuroscience. Front. Syst. Neurosci. *13*, 26.

Koo, B., Choi, B., Park, H., and Yoon, K.J. (2019). Past, present, and future of brain organoid technology. Mol. Cells *42*, 617–627.

Kowalczyk, A.P., and Nanes, B.A. (2012). Adherens junction turnover: regulating adhesion through cadherin endocytosis, degradation, and recycling. Sub-cellular Biochem. *60*, 197–222.

Kreuter, J. (2014). Drug delivery to the central nervous system by polymeric nanoparticles: what do we know? Adv. Drug Deliv. Rev. *71*, 2–14.

Kumarasamy, M., and Sosnik, A. (2019). The nose-to-brain transport of polymeric nanoparticles is mediated by immune sentinels and not by olfactory sensory neurons. Adv. Biosyst. *3*, 1900123.

Kumarasamy, M., and Sosnik, A. (2020). Chapter 11 - overcoming efflux transporter-mediated resistance in cancer by using nanomedicines. In Drug Efflux Pumps in Cancer Resistance Pathways: From Molecular Recognition and Characterization to Possible Inhibition Strategies in Chemotherapy, A. Sosnik and R. Bendayan, eds. (Academic Press), pp. 337–369.

Lawson, L.J., Perry, V.H., and Gordon, S. (1992). Turnover of resident microglia in the normal adult mouse brain. Neuroscience *48*, 405–415.

Lazzari, G., Vinciguerra, D., Balasso, A., Nicolas, V., Goudin, N., Garfa-Traore, M., Feher, A., Dinnyes, A., Nicolas, J., Couvreur, P., et al. (2019). Light sheet fluorescence microscopy versus confocal microscopy: in quest of a suitable tool to assess drug and nanomedicine penetration into multicellular tumor spheroids. Eur. J. Pharm. Biopharm. *142*, 195–203.

Lee, J.H., and Gleeson, J.G. (2010). The role of primary cilia in neuronal function. Neurobiol. Dis. *38*, 167–172.

Lee, C.-T., Bendriem, R.M., Wu, W.W., and Shen, R.-F. (2017). 3D brain Organoids derived from pluripotent stem cells: promising experimental models for brain development and neurodegenerative disorders. J. Biomed. Sci. *24*, 59.

Levine, S., and Grabel, L. (2017). The contribution of human/non-human animal chimeras to stem cell research. Stem Cell Res. *24*, 128–134.

Liu, Z., Li, W., Wang, F., Sun, C., Wang, L., Wang, J., and Sun, F. (2012). Enhancement of lipopolysaccharide-induced nitric oxide and interleukin-6 production by PEGylated gold nanoparticles in RAW264.7 cells. Nanoscale *4*, 7135–7142.

Louvi, A., and Grove, E.A. (2011). Cilia in the CNS: the quiet organelle claims center stage. Neuron *69*, 1046–1060.

Mailänder, V., and Landfester, K. (2009). Interaction of nanoparticles with cells. Biomacromolecules *10*, 2379–2400.

Masaki, H., and Nakauchi, H. (2017). Interspecies chimeras for human stem cell research. Development *144*, 2544–2547.

Matcovitch-Natan, O., Winter, D.R., Giladi, A., Vargas Aguilar, S., Spinrad, A., Sarrazin, S., Ben-Yehuda, H., David, E., Zelada González, F., Perrin, P., et al. (2016). Microglia development follows a stepwise program to regulate brain homeostasis. Science *353*, aad8670.

Meinhardt, J., Radke, J., Dittmayer, C., Mothes, R., Franz, J., Laue, M., Schneider, J., Brünink, S., Hassan, O., Stenzel, W., et al. (2020). Olfactory transmucosal SARS-CoV-2 invasion as port of Central Nervous System entry in COVID-19 patients. Nat. Neurosci. https://doi.org/10.1038/s41593-020-00758-5.

Melief, J., Sneeboer, M.A., Litjens, M., Ormel, P.R., Palmen, S.J., Huitinga, I., Kahn, R.S., Hol, E.M., and de Witte, L.D. (2016). Characterizing primary human microglia: a comparative study with myeloid subsets and culture models. Glia *64*, 1857–1868.

Mergenthaler, P., Lindauer, U., Dienel, G.A., and Meisel, A. (2013). Sugar for the brain: the role of glucose in physiological and pathological brain function. Trends Neurosci. *36*, 587–597.

Author Anonymous. (2018). Method of the year 2017: organoids. Nat. Methods *15*, 1, https://doi.org/10.1038/nmeth.4575.

Moshe Halamish, H., Trousil, J., Rak, D., Knudsen, K.D., Pavlova, E., Nyström, B., Štěpánek, P., and Sosnik, A. (2019). Self-assembly and nanostructure of poly(vinyl alcohol)-graft-poly(methyl methacrylate) amphiphilic nanoparticles. J. Colloid Interface Sci. *553*, 512–523.

Murali, K., Kenesei, K., Li, Y., Demeter, K., Környei, Z., and Madarász, E. (2015). Uptake and bio-reactivity of polystyrene nanoparticles is affected by surface modifications, ageing and LPS adsorption: in vitro studies on neural tissue cells. Nanoscale *7*, 4199–4210.

Naik, P., and Cucullo, L. (2012). In vitro blood-brain barrier models: current and perspective technologies. J. Pharm. Sci. *101*, 1337–1354.

Netto, J.P., Iliff, J., Stanimirovic, D., Krohn, K.A., Hamilton, B., Varallyay, C., Gahramanov, S., Daldrup-Link, H., d'Esterre, C., Zlokovic, B., et al. (2018). Neurovascular unit: basic and clinical imaging with emphasis on advantages of ferumoxytol. Neurosurgery *82*, 770–780.

Noi, I., Schlachet, I., Kumarasamy, M., and Sosnik, A. (2018). Permeability of novel chitosan-g-poly(methyl methacrylate) amphiphilic nanoparticles in a model of small intestine in vitro. Polymers *10*, 478.

Novak, U., and Kaye, A.H. (2000). Extracellular matrix and the brain: components and function. J. Clin. Neurosci. *7*, 280–290.

Nowak, M., Brown, T.D., Graham, A., Helgeson, M.E., and Mitragotri, S. (2020). Size, shape, and flexibility influence nanoparticle transport across brain endothelium under flow. Bioeng. Transl. Med. *5*, e10153.

O'Kane, R.L., Martínez-López, I., DeJoseph, M.R., Viña, J.R., and Hawkins, R.A. (1999). Na(+)-dependent glutamate transporters (EAAT1, EAAT2, and EAAT3) of the blood-brain barrier. A mechanism for glutamate removal. J. Biol. Chem. *274*, 31891–31895.

Ohsawa, K., Imai, Y., Sasaki, Y., and Kohsaka, S. (2004). Microglia/macrophage-specific protein Iba1 binds to fimbrin and enhances its actin-bundling activity. J. Neurochem. *88*, 844–856.

Pampaloni, N.P., Lottner, M., Giugliano, M., Matruglio, A., D'Amico, F., Prato, M., Garrido, J.A., Ballerini, L., and Scaini, D. (2018). Single-layer graphene modulates neuronal communication and augments membrane ion currents. Nat. Nanotechnology *13*, 755–764.

Papaspyropoulos, A., Tsolaki, M., Foroglou, N., and Pantazaki, A.A. (2020). Modeling and targeting Alzheimer's disease with organoids. Front. Pharmacol. *11*, 396.

Pappin, B.B., Kiefel, M.J., and Houston, T.A. (2012). Boron-carbohydrate interactions. In Carbohydrates - Comprehensive Studies on Glycobiology and Glycotechnology, C.F. Chang, ed. (INTECH Open Access), pp. 37–54.

Park, J., Wetzel, I., Marriott, I., Dréau, D., D'Avanzo, C., Kim, D.Y., Tanzi, R.E., and Cho, H. (2018). A 3D human triculture system modeling neurodegeneration and neuroinflammation in Alzheimer's disease. Nat. Neurosci. *21*, 941–951.

Paşca, S.P. (2018). The rise of three-dimensional human brain cultures. Nature *553*, 437–445.

Peng, W., Datta, P., Wu, Y., Dey, M., Ayan, B., Dababneh, A., and Ozbolat, I.T. (2018). Challenges in bio-fabrication of organoid cultures. Adv. Exp. Med. Biol. *1107*, 53–71.

Placone, A.L., McGuiggan, P.M., Bergles, D.E., Guerrero-Cazares, H., Quinones-Hinojosa, A., and Searson, P.C. (2015). Human astrocytes develop physiological morphology and remain quiescent in a novel 3D matrix. Biomaterials *42*, 134–143.

Qosa, H., Miller, D.S., Pasinelli, P., and Trotti, D. (2015). Regulation of ABC efflux transporters at blood-brain barrier in health and neurological disorders. Brain Res. *1628*, 298–316.

Rodriguez-Izquierdo, I., Serramia, M.J., Gomez, R., De La Mata, F.J., Bullido, M.J., and Muñoz-Fernández, M.A. (2020). Gold nanoparticles crossing blood-brain barrier prevent HSV-1 infection and reduce herpes associated amyloid-betasecretion. J. Clin. Med. *9*, 155.

Rommerswinkel, N., Niggemann, B., Keil, S., Zanker, K.S., and Dittmar, T. (2014). Analysis of cell migration within a three-dimensional collagen matrix. J. Vis. Exp. e51963, https://doi.org/10.3791/51963.

Rossi, G., Manfrin, A., and Lutolf, M.P. (2018). Progress and potential in organoid research. Nat. Rev. Genet. *19*, 671–687.

Rowitch, D.H., and Kriegstein, A.R. (2010). Developmental genetics of vertebrate glial-cell specification. Nature *468*, 214–222.

Saraiva, C., Praca, C., Ferreira, R., Santos, T., Ferreira, L., and Bernardino, L. (2016). Nanoparticle-mediated brain drug delivery: overcoming blood-brain barrier to treat neurodegenerative diseases. J. Control. Release *235*, 34–47.

Sarmento, B., Mazzaglia, D., Bonferoni, M.C., Neto, A.P., do Céu Monteiro, M., and Seabra, V. (2011). Effect of chitosan coating in overcoming the phagocytosis of insulin loaded solid lipid nanoparticles by mononuclear phagocyte system. Carbohydr. Polym. *84*, 919–925.

Schlachet, I., and Sosnik, A. (2019). Mixed mucoadhesive amphiphilic polymeric nanoparticles cross a model of nasal septum epithelium in vitro. ACS Appl. Mater. Interfaces *11*, 21360–21371.

Schlachet, I., Trousil, J., Rak, D., Knudsen, K.D., Pavlova, E., Nyström, B., and Sosnik, A. (2019). Chitosan-graft-poly(methyl methacrylate) amphiphilic nanoparticles: self-association and physicochemical characterization. Carbohydr. Polym. *212*, 412–420.

Schlachet, I., Moshe Halamish, H., and Sosnik, A. (2020). Mixed amphiphilic polymeric nanoparticles of chitosan, poly(vinyl alcohol) and poly(methyl methacrylate) for intranasal drug delivery: a preliminary in vivo study. Molecules *25*, 4496.

Seker, M., Fernandez-Rodriguez, C., Martinez-Cruz, L.A., and Müller, D. (2019). Mouse models of human claudin-associated disorders: benefits and limitations. Int. J. Mol. Sci. *20*, 5504.

Sela, H., Cohen, H., Elia, P., Zach, R., Karpas, Z., and Zeiri, Y. (2015). Spontaneous penetration of gold nanoparticles through the blood brain barrier (BBB). J. Nanobiotechnology *13*, 71.

Setyawati, M.I., Tay, C.Y., Bay, B.H., and Leong, D.T. (2017). Gold nanoparticles induced endothelial leakiness depends on particle size and endothelial cell origin. ACS Nano *11*, 5020–5030.

Simian, M., and Bissell, M.J. (2017). Organoids: a historical perspective of thinking in three dimensions. J. Cell Biol. *216*, 31–40.

Simpson, I.A., Dwyer, D., Malide, D., Moley, K.H., Travis, A., and Vannucci, S.J. (2008). The facilitative glucose transporter GLUT3: 20 years of distinction. Am. J. Physiol. Endocrinol. Metab. *295*, E242–E253.

Singh, M.R. (2018). Application of metallic nanomaterials in nanomedicine. Adv. Exp. Med. Biol. *1052*, 83–102.

Sipos, É., Komoly, S., and Ács, P. (2018). Quantitative comparison of primary cilia marker expression and length in the mouse brain. J. Mol. Neurosci. *64*, 397–409.

Sivandzade, F., and Cucullo, L. (2018). In-vitro blood-brain barrier modeling: a review of modern and fast-advancing technologies. J. Cereb. Blood Flow Metab. *38*, 1667–1681.

Smith, J.N., Thomas, D.G., Jolley, H., Kodali, V.K., Littke, M.H., Munusamy, P., Baer, D.R., Gaffrey, M.J., Thrall, B.D., and Teeguarden, J.G. (2018). All that is silver is not toxic: silver ion and particle kinetics reveals the role of silver ion aging and dosimetry on the toxicity of silver nanoparticles. Part. Fibre Toxicol. *15*, 47.

Stamatovic, S.M., Johnson, A.M., Keep, R.F., and Andjelkovic, A.V. (2016). Junctional proteins of the blood-brain barrier: new insights into function and dysfunction. Tissue Barriers *4*, e1154641.

Suidan, G.L., Brill, A., De Meyer, S.F., Voorhees, J.R., Cifuni, S.M., Cabral, J.E., and Wagner, D.D. (2013). Endothelial Von Willebrand factor promotes blood-brain barrier flexibility and provides protection from hypoxia and seizures in mice. Arterioscler. Thromb. Vasc. Biol. *33*, 2112–2120.

Szepesi, Z., Manouchehrian, O., Bachiller, S., and Deierborg, T. (2018). Bidirectional microglia–neuron communication in health and disease. Front. Cell. Neurosci. *12*.

Tam, S.J., and Watts, R.J. (2010). Connecting vascular and nervous system development: angiogenesis and the blood-brain barrier. Annu. Rev. Neurosci. *33*, 379–408.

Tang, J., Xiong, L., Zhou, G., Wang, S., Wang, J., Liu, L., Li, J., Yuan, F., Lu, S., Wan, Z., et al. (2010). Silver nanoparticles crossing through and distribution in the blood-brain barrier in vitro. J. Nanoscience Nanotechnology *10*, 6313–6317.

Tang, W., Fan, W., Lau, J., Deng, L., Shen, Z., and Chen, X. (2019). Emerging blood-brain-barrier-crossing nanotechnology for brain cancer theranostics. Chem. Soc. Rev. *48*, 2967–3014.

Trujillo, C.A., Gao, R., Negraes, P.D., Gu, J., Buchanan, J., Preissl, S., Wang, A., Wu, W., Haddad, G.G., Chaim, I.A., et al. (2019). Complex oscillatory waves emerging from cortical organoids model early human brain network development. Cell Stem Cell *25*, 558–569.e7.

Tsuji, A. (2005). Small molecular drug transfer across the blood-brain barrier via carrier-mediated transport systems. NeuroRX *2*, 54–62.

Uchegbu, I., Wang, Z., Xiong, G., Tsang, A., and Schatzlein, A. (2019). Nose to brain delivery. J. Pharmacol. Exp. Ther. *370*, 593–601.

Urich, E., Patsch, C., Aigner, S., Graf, M., Iacone, R., and Freskgard, P.O. (2013). Multicellular self-assembled spheroidal model of the blood brain barrier. Scientific Rep. *3*, 1500.

Walchli, T., Wacker, A., Frei, K., Regli, L., Schwab, M.E., Hoerstrup, S.P., Gerhardt, H., and Engelhardt, B. (2015). Wiring the vascular network with neural cues: a CNS perspective. Neuron *87*, 271–296.

Wang, L., Pavlou, S., Du, X., Bhuckory, M., Xu, H., and Chen, M. (2019). Glucose transporter 1 critically controls microglial activation through facilitating glycolysis. Mol. Neurodegeneration *14*, 2.

Watson, P.M.D., Kavanagh, E., Allenby, G., and Vassey, M. (2017). Bioengineered 3D glial cell culture systems and applications for neurodegeneration and neuroinflammation. SLAS Discov. *22*, 583–601.

Weksler, B., Romero, I.A., and Couraud, P.O. (2013). The hCMEC/D3 cell line as a model of the human blood brain barrier. Fluids Barriers CNS *10*, 16.

Wilt, B.A., Burns, L.D., Wei Ho, E.T., Ghosh, K.K., Mukamel, E.A., and Schnitzer, M.J. (2009). Advances in light microscopy for neuroscience. Annu. Rev. Neurosci. *32*, 435–506.

Wolburg, H., Wolburg-Buchholz, K., Liebner, S., and Engelhardt, B. (2001). Claudin-1, claudin-2 and claudin-11 are present in tight junctions of choroid plexus epithelium of the mouse. Neurosci. Lett. *307*, 77–80.

Yang, Z., Liu, Z.W., Allaker, R.P., Reip, P., Oxford, J., Ahmad, Z., and Ren, G. (2010). A review of nanoparticle functionality and toxicity on the central nervous system. J. R. Soc. Interface *7*, S411–S422.

Yang, W., Cai, S., Yuan, Z., Lai, Y., Yu, H., Wang, Y., and Liu, L. (2019). Mask-free generation of multicellular 3D heterospheroids array for high-throughput combinatorial anti-cancer drug screening. Mater. Des. *183*, 108182.

Yip, D., and Cho, C.H. (2013). A multicellular 3D heterospheroid model of liver tumor and stromal cells in collagen gel for anti-cancer drug testing. Biochem. Biophys. Res. Commun. *433*, 327–332.

Zaritski, A., Castillo-Ecija, H., Kumarasamy, M., Peled, E., Sverdlov Arzi, R., Carcaboso, Á.M., and Sosnik, A. (2019). Selective accumulation of galactomannan amphiphilic nanomaterials in pediatric solid tumor xenografts correlates with GLUT1 gene expression. ACS Appl. Mater. Interfaces *11*, 38483–38496.

Zhao, Y., Xin, Y., He, Z., and Hu, W. (2018). Function of connexins in the interaction between glial and vascular cells in the central nervous system and related neurological diseases. Neural Plasticity *2018*, 6323901.

Zheng, P.-P., Romme, E., van der Spek, P.J., Dirven, C.M.F., Willemsen, R., and Kros, J.M. (2010). Glut1/SLC2A1 is crucial for the development of the blood-brain barrier in vivo. Ann. Neurol. *68*, 835–844.

Zhou, Y., Peng, Z., Seven, E.S., and Leblanc, R.M. (2018). Crossing the blood-brain barrier with nanoparticles. J. Control. Release *270*, 290–303.

Zlokovic, B.V. (2008). The blood-brain barrier in health and chronic neurodegenerative disorders. Neuron *57*, 178–201.

iScience, Volume *24*

Supplemental information

Heterocellular spheroids of the neurovascular blood-brain barrier as a platform for personalized nanoneuromedicine

Murali Kumarasamy and Alejandro Sosnik

Supplementary Figures and Tables

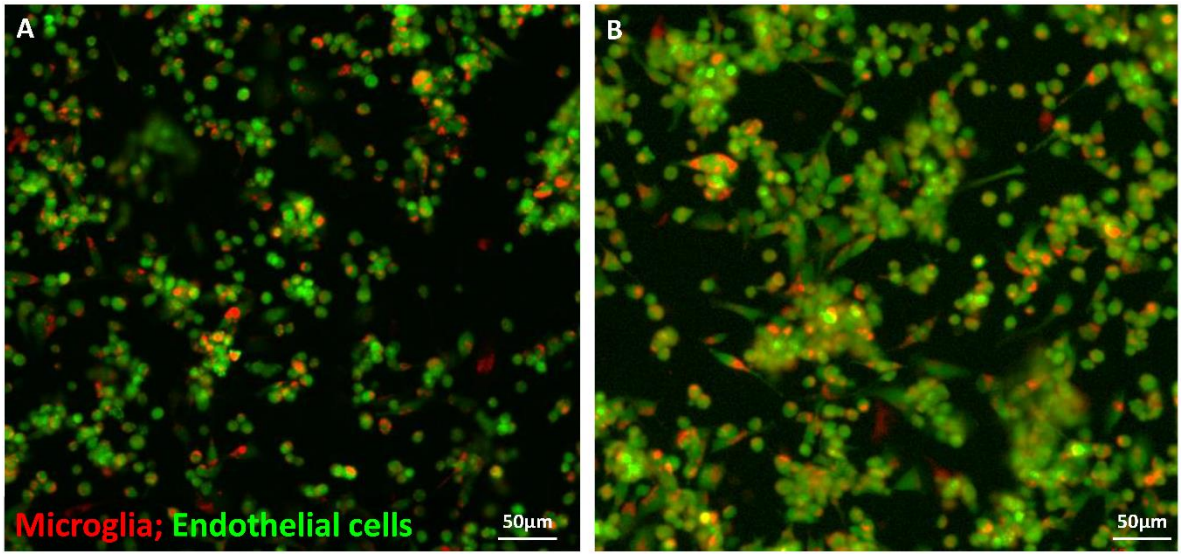

Figure S1. Interspecies interaction of human and rat cells. Related to Figure 1.
CLSFM micrographs of hCMEC/D3 endothelial cells (green) and primary rat microglia (red) stained with Cell Tracking Dye Kit - Green - Cytopainter and Cell Tracking Dye Kit - Deep Red – Cytopainter, respectively, after (A) 1 h and (B) 12 h.

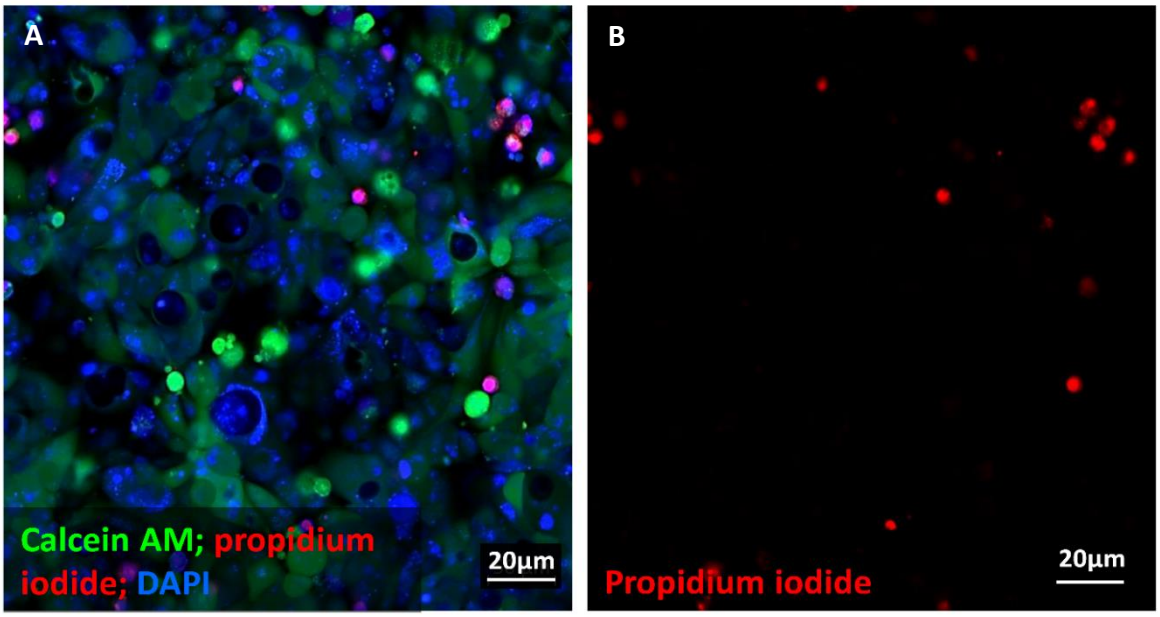

Figure S2. Five-cell spheroid viability. Related to Figure 2.
CLSFM micrographs of 5-cell spheroids stained with (A) calcein AM (live cells, green) and propidium iodide (dead cells, red) and (B) propidium iodide (dead cells, red). Cell nuclei in B-F are stained with 4′,6-diamidino-2-phenylindole (DAPI, blue).

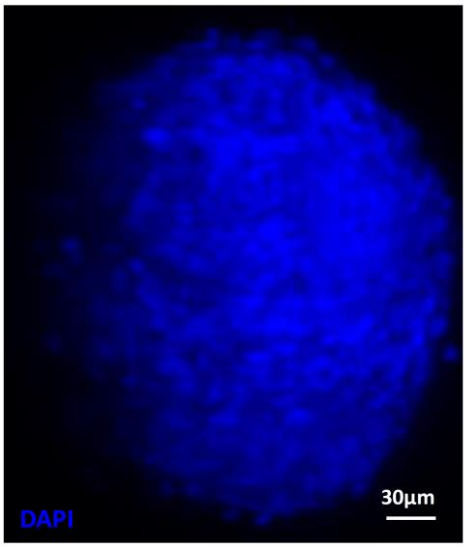

Figure S3. Characterization of the solid cell structure of 5-cell spheroids. Related to Figure 3.
LSFM micrograph of a spheroid showing nuclei of all the cells stained with DAPI (blue).

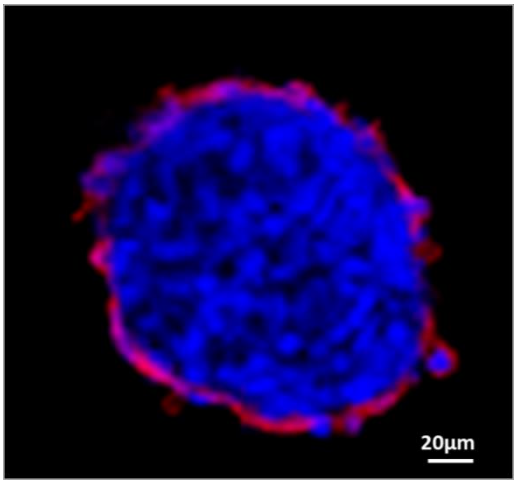

Figure S4. Characterization of hCMEC/D3 endothelial cell distribution in 5-cell spheroids. Related to Figure 3.
CLSFM micrograph of a spheroid showing endothelial cells immunostained for VE-cadherin (red) and nuclei of all the cells stained with DAPI (blue).

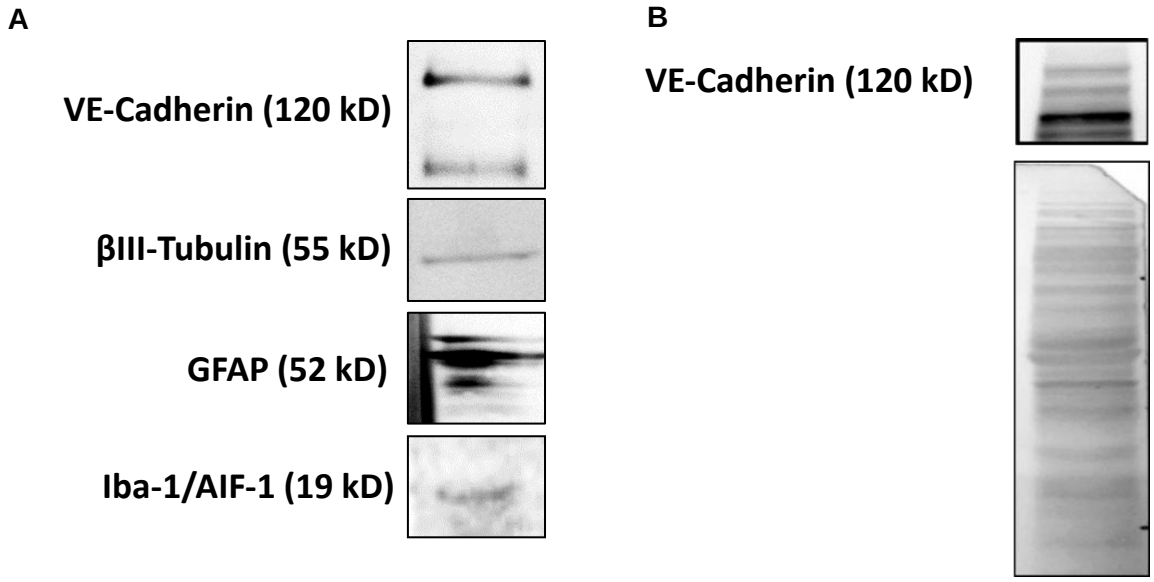

Figure S5. Western blotting analysis of brain specific neurovascular spheroids. Related to Figure 3.
Confirmation of the expression of characteristic protein markers.

Table S1. Quality control of a high-quality total RNA sample by using 1% agarose gel electrophoresis. Related to Figure 6.

Sample number	Sample name	Concentration, (ng/μL) [a]	RIN (TS)
1	Endothelial cells 2D	264	8.5
2	Endothelial cells 2D	116	10
3	Endothelial cells 2D	266	8.5
4	Endothelial cells 3D	110	9.6
5	Endothelial cells 3D	106	9.7
6	Endothelial cells 3D	111	9.6
7	Human 3-cell organoid	69.4	10
8	Human 3-cell organoid	99.4	10
9	Human 3-cell organoid	62.6	10

[a] Determined by Qubit®.
Note: RNA with excellent quality, RIN = 10; RNA with acceptable quality, RIN = 6.9; RNA with poor quality, RIN = 1.8.

Table S2. Technical information and quality of sequencing. Related to Figure 6.

			Quality of Run				
Lane	**Sample**	**Index**	**Control - Mapped (%)**	**Control - Mismatch (%)**	**PF reads (%)**	**Unknown reads (%)**	**Number PF reads**
8	BBB organoids	AGTCAA					25,990,463
		AGTTCC					24,495,706
		GTGGCC					21,842,753
	ECs 2D flat culture	ATGTCA					25,571,133
		CCGTCC	1.46	0.06	91.95	2.18	27,419,486
		GTTTCG					26,094,770
	EC 3D organoids	GTCCGC					25,944,636
		GTGAAA					25,979,188
		CGTACG					22,945,300

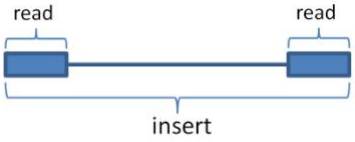

- **Insert** – the DNA/cDNA sequence located between sequencing adapters.

  Read – one end of the paired-end segments.

- **Control -** PhiX is a bacteriophage with a known genome sequence that is used as a standard sequencing control to estimate read accuracy. 1-2% of the reads of each lane are comprised of a PhiX sample which is mapped to the PhiX genome to estimate the error rate and quality of the sequencing run. A good control would have approximately 1% mapped control reads, and up to 1% mismatches (error rate).

- **Unknown reads -** an adapter containing a sample specific barcode is added to each library during library preparation. In some cases, if a read's sequenced barcode contains sequencing errors, then the read cannot be specifically identified with any sample and it is considered as "unknown". The percentage reported in the table is out of the total number of reads per lane.

- **PF** (Passed Filter) **-** indicates reads that passed the automatic quality filter of the sequencer.

Table S3. Trimming statistics. Related to Figure 6.

Sample	Total reads	Containing adapter (%) Reads	Trimmed bases (%)	Reads removed (%)	Reads removed (#)
3-cell BBB organoids	25,990,463	2.6	0.3	0.1	18,349
	24,495,706	2.6	0.3	0.1	17,334
	21,842,753	2.6	0.3	0.1	17,212
ECs 2D-culture	25,571,133	2.6	0.3	0.1	17,660
	27,419,486	2.7	0.3	0.1	19,354
	26,094,770	2.7	0.3	0.1	17,324
EC 3D-organoids	25,944,636	2.7	0.3	0.1	24,616
	25,979,188	2.6	0.3	0.1	21,511
	22,945,300	2.6	0.3	0.1	16,927

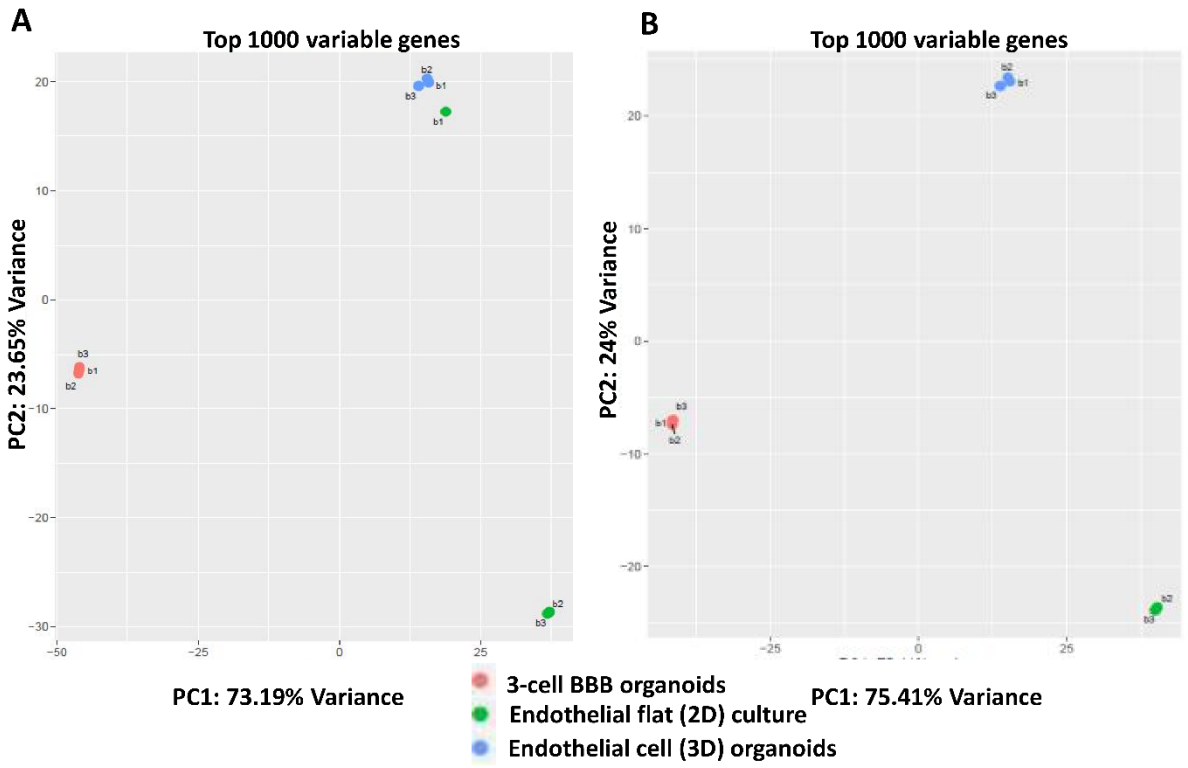

Figure S6. Identification of genes that are most informative for defining cell subpopulations by PCA. Related to Figure 6.
(A) PCA plot between the three groups and (B) PCA plot between groups, after excluding the outlier sample of endothelial flat (2D) culture.

Table S4. Mapping statistics. Related to Figure 6.

Sample	**Total no reads**	% unmapped	% Uniquely unmapped	# Uniquely unmapped	% Multi Mapped	% Gapped Uniquely mapped reads (out of unique)
BBB organoids	25,972,114	1.99	95.12	24,703,511	2.9	20.32
	24,478,372	2.05	95.12	23,283,509	2.83	19.99
	21,825,541	2	95.2	20,777,273	2.8	20.2
ECs 2D flat culture	25,553,473	1.89	95.28	24,347,151	2.84	20.65
	27,400,132	2.56	94.09	25,780,893	3.35	16.81
	26,077,446	2.64	93.87	24,479,978	3.48	16.64
EC 3D organoids	25,920,020	2.15	94.1	24,390,672	3.75	18.86
	25,957,677	2.09	94.65	24,570,220	3.26	19.04
	22,928,373	2.12	94.5	21,668,202	3.38	18.68

•**Uniquely mapped** – Reads aligned with high confidence to a single genomic location with up to 2 mismatches. Only the uniquely mapped reads are used for further analysis.

•**Unmapped** – Reads for which no alignment was found to the reference genome.

•**Multi-mapped** – Reads mapped to more than one possible location in the genome. These reads are not used in the analysis.

•**Gapped uniquely mapping** – Reads aligned uniquely to a splice junction **(Figure. 3)**

Table S5. Differential expression analysis of endothelial cells in 3-human cell spheroids, endothelial cell (3D) spheroids and endothelial cell flat (2D) cultures. Related to Figure 6.
Pairwise testing between conditions.

Comparison	**Total # Genes**	**All Zero**	**Low Counts**	**Tested**	**Significant up-regulation**	**Significant down-regulation**
3-Human cell spheroids vs._ endothelial cell flat (2D) cultures	58,174	22,654	15,211	20,309	7314	6273
3-Human cell spheroids vs._ endothelial cell (3D) spheroids	58,174	22,654	16,294	19,226	3966	3487
Endothelial cell flat (2D) cultures vs._ endothelial cell (3D) spheroids	58,174	22,654	15,849	19,671	6290	6503

Table S6. Comparative expression of different characteristic genes of endothelial cells in 3-human cell spheroids, endothelial cell (3D) spheroids and endothelial cell flat (2D) cultures, as determined by RNA-Seq. Related to Figure 6.

Gene	3-Human cell spheroids vs. endothelial cell flat (2D) cultures	3-Human cell spheroids vs. endothelial cell (3D) spheroids	Endothelial cell flat (2D) cultures vs. endothelial cell (3D) spheroids
GJA1	Upregulated	Upregulated	Downregulated
EDN1	Upregulated	Upregulated	Downregulated
VWF	Upregulated	Downregulated	Downregulated
CD34	Upregulated	Downregulated	Downregulated
ENG	Upregulated	Upregulated	Downregulated
VCAM1	Upregulated	No change	Downregulated
EMCN	Upregulated	Upregulated	No change
NR2F2	Upregulated	Upregulated	Downregulated
CDH5	Upregulated	Downregulated	Downregulated
GJA4	No change	No change	No change
EPHB4	Upregulated	Downregulated	Downregulated
MCAM	Upregulated	Upregulated	Downregulated
FLT1	No change	Downregulated	No change
NOS3	No change	No change	No change
FLT4	No change	No change	No change
PTPRC	No change	No change	No change
CD4	Upregulated	Upregulated	No change
ICAM3	No change	No change	No change
BCL6	Upregulated	Upregulated	Upregulated
CD28	No change	No change	No change
ITGA4	Up	Upregulated	Downregulated
CD38	No	Upregulated	No change
CD86	No	No change	No change
MS4A1	No	No change	No change

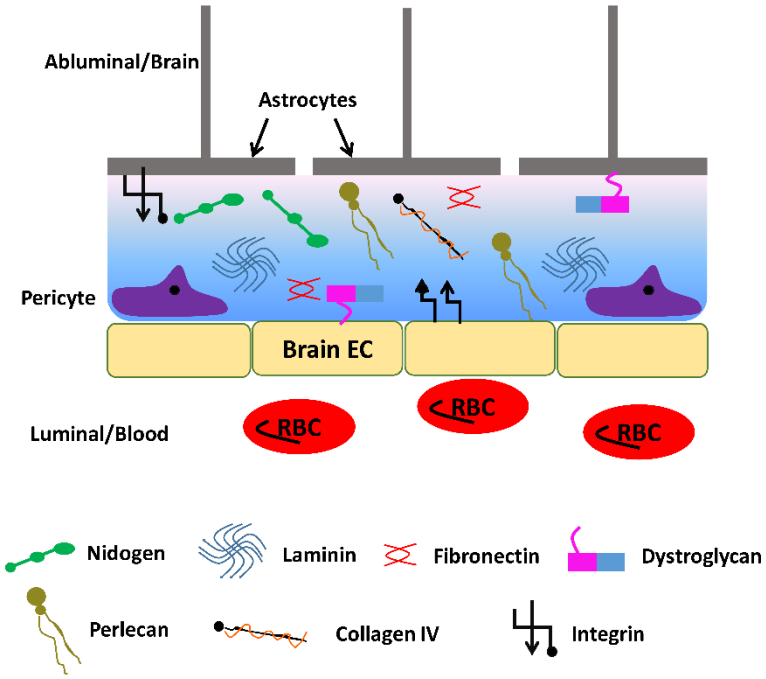

Figure S7. Scheme of the extracellular matrix (ECM) in the vascular and parenchymal basement membrane of endothelial cells (EC) and red blood cells (RBC). Related to Figure 6.
Key proteins are indicated.

Table S7. Properties of the different polymeric, metallic and carbon nanoparticles used to investigate the interaction of nanomaterials with 5-cell spheroids. Related to Figures 7 and 8.

Nanoparticle type	D_h (nm) ± S.D.	PDI	Z-potential (mV)	Nanoparticle description
Polymeric				
CS-PMMA33	188 ± 9	0.30	+23.0	Non-crosslinked amphiphilic nanoparticles produced by the self-assembly of a graft copolymer of chitosan (CS) and poly(methyl methacrylate) (PMMA) containing 33% w/v of PMMA (Noi et al., 2018)
Crosslinked mixed CS-PMMA30:PVA-PMMA17	463 ± 73	0.55	+3.0	Mixed amphiphilic nanoparticles produced by the self-assembly of a 1:1 weight ratio mixture of a graft copolymer of chitosan (CS) and poly(methyl methacrylate) (PMMA) containing 30% w/v of PMMA and a graft copolymer of poly(vinyl alcohol) (PVA) and PMMA containing 17% w/v of PMMA. Nanoparticles were ionotropically crosslinked with sodium

				tripolyphosphate which reacts with CS domains (Schlachet and Sosnik, 2019)
Crosslinked PVA-PMMA17	92 ± 4	0.14	-14.6	Amphiphilic nanoparticles produced by the self-assembly of a graft copolymer of poly(vinyl alcohol) (PVA) and poly(methyl methacrylate) (PMMA) containing 17% w/v of PMMA (Moshe Halamish et al., 2019). Nanoparticles were non-covalently crosslinked with boric acid which reacts with PVA domains (Moshe Halamish et al., 2019)
hGM-PMMA28	141 ± 3	0.11	-0.4	Amphiphilic nanoparticles produced by the self-assembly of a graft copolymer of hydrolyzed galactomannan (hGM) and poly(methyl methacrylate) (PMMA) containing 28% w/v of PMMA (Zaritski et al., 2019)
Metallic				
Silver	60 ± 13		-38.0	An aqueous solution of silver nitrate was heated to boiling, sodium citrate and sodium borohydride was

				added slowly (Bastús et al., 2014; Quintero-Quiroz et al., 2019)
Gold	10 ± 2	<0.20	-17.8	Commercially available
Ceramic				
Graphene nanoplatelets	~5 µm diameter and 10 nm thickness	-	-	Commercially available
Alkaline carbon dots	10 ± 3	0.20	−12.0 mV	Sodium hydroxide was mixed with acetone under vigorous magnetic stirring for 1 h, and then the mixture was placed at ambient air, temperature, and pressure. The product was separated by centrifugation and washed to get a powder of alkaline quantum dots (Hou et al., 2015).

Figure S8. Per-base quality scores. Related to Figure 6.

Table S8. Read assignments according to gene annotations. Related to Figure 6.

Sample	**# reads unique**	% reads unique	# no feature	% no feature	Number ambiguous	%ambiguous
BBB organoids	21,478,458	86.94	1,734,480	7.02	1,490,573	6.03
	20,218,632	86.84	1,679,234	7.21	1,385,643	5.95
	18,066,504	86.95	1,453,586	7	1,257,183	6.05
ECs 2D flat culture	21,637,878	88.87	1,182,240	4.86	1,527,033	6.27
	21,594,711	83.76	2,686,051	10.42	1,500,131	5.82
	20,471,953	83.63	2,580,918	10.54	1,427,107	5.83
EC 3D organoids	20,884,278	85.62	2,006,406	8.23	1,499,988	6.15
	21,168,497	86.16	1,863,925	7.59	1,537,798	6.26
	18,520,642	85.47	1,809,475	8.35	1,338,085	6.18

•**Counted reads** – uniquely mapped reads assigned to annotated exons.

•**No feature** – reads that could not be assigned to any annotated gene.

•**Ambiguous –** reads that can be assigned to more than one annotated gene and are therefore not counted to any gene.

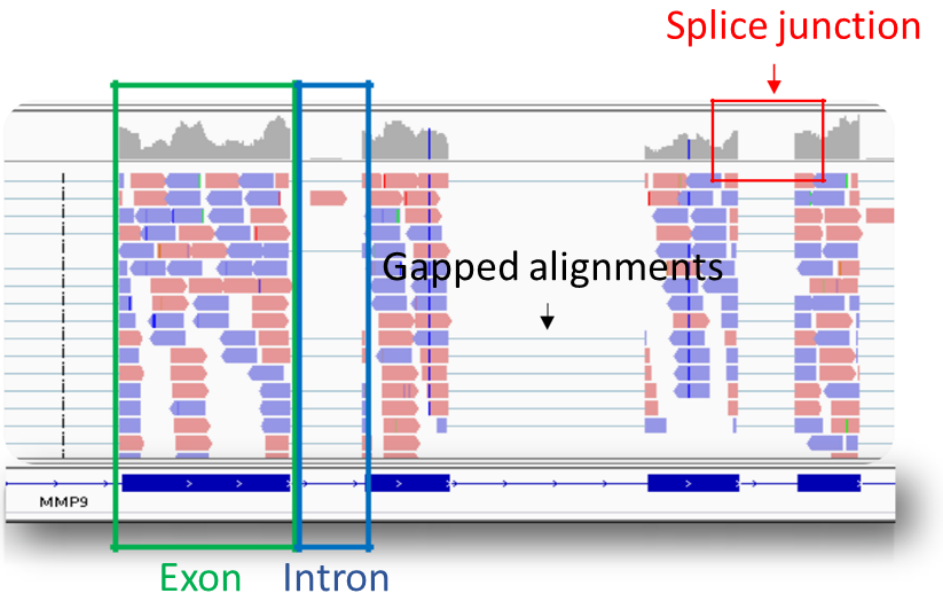

Figure S9. Illustration of RNA-Seq read alignments using Tophat2 – A graphic representation of the mapping patterns of RNA-Seq reads to a reference genome. Related to Figure 6.
The figure above reveals the distribution of reads that are mapped to exons (outlined in green), a splice junction (outlined in red), and introns (outlined in blue). The figure allows the user to see that the majority of reads map to exons, slightly fewer reads map in a gapped manner to the pictured splice junction, and—consistent with the nature of RNA library preparation preference for mature mRNAs—almost no reads map to introns.

Transparent Methods

Cell cultures

The hCMEC/D3 cell line derived from human temporal lobe microvessels (hBMECs, EMD Millipore, Burlington, MA, USA) was maintained in EndoGRO Basal Medium (EMD Millipore) with supplements containing 5% fetal bovine serum (FBS), L-glutamine, vitamin C, heparin sulfate and recombinant human epidermal growth factor (*rhEGF*), all purchased from Sigma-Aldrich (St. Louis, MO, USA). hAs (ScienCell Research Laboratories, Carlsbad, CA, USA) were grown in astrocyte growth medium (ScienCell Research Laboratories) containing 2% FBS supplemented with astrocyte growth factors, penicillin-streptomycin (Brissette et al., 2013) hBVPs (ScienCell Research Laboratories) were maintained in pericyte culture medium (ScienCell Research Laboratories) containing 2% FBS, pericyte growth supplement and penicillin-streptomycin (Neuhaus et al., 2017). All cells were incubated at 37°C in humidified 5% CO_2/95% air.

Animals and isolation of primary neural-tissue cells

The use of neonate Sprague-Dawley (SD) rats (P0-1) and the protocols utilized for the isolation of the primary CNS cells were conducted with the approval of the Animal Care Committee of the Technion-Israel Institute of Technology. All the experimental procedures were in accordance with the guidelines set by the EU Council Directive (86/609 EEC) and according to the official protocol #IL-141-10-17 (expiry date 19 December 2021).

Primary neural, and neural stem/progenitor cells (Beaudoin et al., 2012; Seibenhener and Wooten, 2012) were isolated from P0-1 SD rats. Briefly, rats were sacrificed by decapitation, and whole brains were quickly removed aseptically (SZ09010122 Binocular Zoom Stereo Microscope, 8x~50x, YSC Technologies, Fremont, CA, USA). Cerebral cortices of three pups were dissected under sterile conditions and kept on ice in a sterile Falcon tube (15 mL) containing 3 mL of trypsin-EDTA 0.25% (Sigma-Aldrich) for 10 min. The enzyme solution was aspirated, and enzyme-digested tissues were triturated in 10 mL of warm (37°C) Dulbecco's Modified Eagle Medium *(*DMEM, Sigma-Aldrich) containing 10% heat-inactivated FBS. Cortical neuron cultures were dissociated by trituration using a 10 mL pipette (about 15-20 times) and cells were centrifuged (Z300 Hermle Micro Centrifuge, Hermle AG, Gosheim, Germany) at 4°C (1500g, 5 min) to obtain pellets. Single cells were separated from non-dissociated tissue debris by sieving them through Falcon™ Cell Strainers (pore diameter of 70μm, Sigma-Aldrich) and seeded onto 24- or 96-well plates coated with poly-L-lysine-

(PLL, Sigma-Aldrich) at cell densities of 2×10^5 or 1×10^4 cells/well, respectively. Cultures were incubated at 37°C in a humidified atmosphere of 5% CO_2/95% air. Cultured cells were grown in serum-free neuron-specific DMEM and Ham's F12 nutrient mixture (DMEM: F12 1:1, Sigma-Aldrich) supplemented with 1% v/v insulin-transferrin-selenite (ITS, Sigma-Aldrich). For conventional cultures and bioimaging, the dissociated cultures were plated on glass coverslips in 24-well plates (Paul Marienfeld GmbH & Co. KG., Lauda-Königshofen, Germany). Before culture, glass coverslips were washed in water and 96% ethanol, air-dried, placed in 24-well plates, and coated with PLL overnight. The cell composition of the cultures was characterized by immunocytochemical staining for neuron specific biomarkers. Microglial cultures were prepared according to Saura *et al.* (Saura et al., 2003). Briefly, P0-1 SD rat brains were removed and rinsed in phosphate buffer saline (PBS, Sigma-Aldrich). After careful removal of the meninges and brains cortices, they were mechanically dissociated and trypsinized for 20 min. Cells were cultured in 6-well plates with DMEM containing 10% FBS at 37°C in humidified 5% CO_2/95% air. The medium was exchanged twice weekly. Microglia cells were isolated from mixed glia by mild trypsinization (30 min-2 h) with trypsin-EDTA 0.25% diluted 1:3 in serum-free DMEM, at 37°C. After detachment of astrocyte brown sheets, the firmly attached macrophages were further propagated in DMEM:F12 1:1 with 10% FBS and the cells replated in 24-well plates containing PLL-coated glass coverslips at a density of 50,000 cells/well. For microglia stainings, cells were fixed and the immunostaining and imaging were performed according to the protocol described below.

Assembly of heterocellular spheroids

Three-cell spheroids comprising hCMEC/D3, hAs and hBVPs were cultured in EndoGRO Basal Medium supplemented with 5% FBS, L-glutamine, vitamin C, heparin sulfate and rhEGF, at 37°C in humidified 5% CO_2/95% air using the liquid overlay culture system. We used the same method to produce 5-cell spheroids incorporating primary neurons and microglia isolated from neonate rat (see above). This method is our adaptation of the aggregate cultures previously described (Johnstone et al., 1998). Briefly, the three or five cell types were harvested by trypsin-EDTA 0.25% and resuspended in ENDOGro culture medium. The concentration of hECs, hAs, hBVPs, primary neurons and microglia cells in each individual suspension was determined using a haemocytometer. Then, cells were resuspended in 100 µL of medium at a 4:2:1:1:1 ratio and transferred to ultralow attachment (ULA) round bottom 96-well plates (CellCarrier Spheroid ULA 96-well Microplates, PerkinElmer, Waltham, MA, USA). In another method, we prepared a 1% w/v agarose solution (molecular biology grade, Bio-Rad

Laboratories, Hercules, CA, USA) in PBS under boiling until complete dissolution. The agarose solution (100 μL) was pipetted into each well of a 96-well plate, while it was still hot, and allowed to cool to 37°C and solidify. Then, a suspension of 5-cell spheroids contains hCMEC/D3, hAs, hBVPs, and primary neurons and microglia cells at a 4:2:1:1:1 ratio and hCMEC/D3 endothelial cells, hAs and hBVPs (1:1:1 ratio), was seeded in the 96-well plate. In both methods, cells were incubated in ENDOGro medium, at 37°C in humidified 5% CO_2/95% air for 48–72 h to allow the formation of the spheroids, as exemplified for a 5-cell spheroid produced in round bottom 96-well plate in **Video S1**.

To rule out possible detrimental human-rodent cell interactions during spheroid assembly, hCMEC/D3 and primary rodent microglia cells were labeled with Cell Tracking Dye Kit - Green - Cytopainter (ab138891, Abcam, Cambridge, UK) and Cell Tracking Dye Kit - Deep Red - Cytopainter (ab138894, Abcam), respectively, and imaged by a GE InCell Analyzer 2000 Imaging System (GE Healthcare, Chicago, IL, USA). For the staining, cells were mixed with each dye (1:1000 dilution in PBS) for 10 min, at 37°C in humidified 5% CO_2/95% air, washed thrice with ENDOGro culture medium and co-cultured on CellCarrier Spheroid ULA 96-well Microplates to form 2-cell spheroids. Images were acquired with a 10x objective at the end of each illumination period (every 10 min) for 12 h.

Characterization of heterocellular spheroids

LIVE/DEA assay

Heterocellular spheroids were resuspended at day 3, the cell viability was determined by using a calcein-AM/propidium iodide LIVE/DEAD assay and nuclei stained with DAPI (all supplied by Sigma-Aldrich). Briefly, the cell culture medium was removed and 1 μM calcein AM and 1.5 μM propidium iodide were added in each well, and the spheroids gently resuspended and incubated for 20 min, at 37°C. Spheroids were visualized by CLSFM (LSM 710 microscope, Carl Zeiss AG, Oberkochen, Germany). Fluorescence mean intensities of both live and dead cells were estimated by ImageJ software (National Institutes of Health, MD, USA).

Immunofluorescent labeling

Spheroids and monocultures were collected at day 5, pooled into a 0.2 mL Eppendorf tube (Corning Inc., Corning, NY, USA), washed thrice (5 min) with PBS and fixed in 4% w/v paraformaldehyde (PFA, Sigma-Aldrich) for 15 min at room temperature (RT). Fixed spheroids were washed twice in PBS, permeabilized with 0.1% w/v Triton X-100 (Sigma-

Aldrich) solution in PBS and blocked with 1% w/v bovine serum albumin (BSA, Sigma-Aldrich) for 1 h. Then, spheroids were incubated in mixtures of primary antibodies overnight at RT under constant rotation, washed thrice with PBS, incubated overnight at 4°C in a mixture of secondary antibodies, all diluted in blocking solutions. Finally, the remainders of secondary antibodies were washed with PBS before staining cell nuclei with DAPI.

Immunolabeled spheroids were visualized by using a LSM 710 microscope equipped with 10x, 20x, 40× water 1.4 NA and 63× oil (numerical aperture:1.3) Carl Zeiss objectives (as indicated in the corresponding figure legends). We used 405, 488, 561 and 647 nm lasers, and the scanning was done in line serial mode, pixel size was 50 x 50 nm. Image stacks were obtained with Zen Elements software. Whole-spheroid images were acquired using a 10× magnification objective and images were processed by using the Zen 100 software.

The following commercial primary antibodies were used at a concentration of 1:500: (i) βIII-tubulin (AA10, sc-80016; Santa Cruz Biotechnology, Inc., Dallas, TX, USA), (ii) GFAP (sc-33673, Santa Cruz), (iii) AQP4 (sc-390488 Santa Cruz), (iv) CLDN5 (sc-374221, Santa Cruz), (v) Iba-1/AIF-1 (sc-32725, Santa Cruz), (vi) VE-cadherin (ab33168, Abcam), (vii) iNOS (ab15323; Abcam), (viii) MAP-2 (sc-74421, Santa Cruz), and (ix) NG2 (sc-53389, Santa Cruz). The following commercial secondary antibodies were used at a concentration of 1:1000: (i) goat anti-rabbit IgG H&L (Alexa Fluor® 594, ab150080, Abcam), (ii) mouse IgG kappa binding protein (m-IgGκ BP) conjugated to CruzFluor™ 488 (sc-516176, Santa Cruz), (iii) mouse IgG kappa binding protein (m-IgGκ BP) conjugated to CruzFluor™ 555 (sc-516177, Santa Cruz), and (iv) mouse IgG kappa binding protein (m-IgGκ BP) conjugated to CruzFluor™ 647.

This method was also used to characterize the permeability of selected polymeric NPs and their localization within the spheroid. For this, NPs were synthesized by utilizing copolymers fluorescently-labeled by the conjugation of fluorescein isothiocyanate (FITC, green fluorescence, Sigma-Aldrich) or rhodamine isothiocyanate (RITC, red fluorescence Sigma-Aldrich) (Moshe Halamish et al., 2019; Noi et al., 2018; Schlachet and Sosnik, 2019; Zaritski et al., 2019).

Electron microscopy

Spheroids were established for 24-72 h and collected and pooled in an Eppendorf tube. Then, they were washed once with PBS, and immersed in modified Karnovsky's fixative (2% w/v glutaraldehyde and 3% w/v PFA in 0.1 M sodium cacodylate buffer containing 5mM $CaCl_2$

and 3% sucrose, all from Sigma-Aldrich) for 1 h at RT. Spheroids were washed in 0.1 M cacodylate buffer and fixed with 1% w/v osmium tetroxide (Sigma-Aldrich)/0.5% w/v potassium dichromate (1 h), stained with 1% w/v uranyl acetate (1 h), washed twice with water and dehydrated in ethanol (Bio-Lab Ltd., Jerusalem, Israel) according to the following sequence: 50% (10 min), 70% (10 min), 90% (10 min) and 100% (2 × 10 min). Samples were embedded in EMbed 812 resin (Electron Microscopy Sciences, Hatfield, PA, USA) and polymerized at 60°C for 48 h (Douglas and Elser, 1972; Murray et al., 1991; Phillips, 1998). Ultrathin sections (~70 nm) were produced in an ultra-microtome (Leica Biosystems, Buffalo Grove, IL, USA), transferred to copper grids (Sigma-Aldrich) and visualized by using a Zeiss Ultra-Plus FEG-SEM (Carl Zeiss AG) equipped with STEM detector at accelerating voltage of 30 kV. This method was also used to characterize the permeability and the intracellular fate of model metallic and ceramic NPs in the spheroids and enabled the elucidation of ultrastructural details and mechanisms of NP–spheroid interactions.

Light sheet fluorescence microscopy

Spheroids fixed in 4% w/v PFA and immunostained were embedded in 1% w/v low melting agarose (Bio-Rad Laboratories) solution and placed in an Eppendorf tube. Samples were analyzed by using a ZEISS Lightsheet Z.1 Fluorescence Microscope (Carl Zeiss) with the Sampler Starter Kit containing four color coded sleeves with their corresponding plungers to fit the glass capillaries high optical clarity for the 3D imaging to the sample holder. Upon selection of the proper capillary based on the sample size and plunger assembly, a 1% w/v low melting agarose solution (100 μL) in sterile PBS was mixed with the spheroid, plunged into the capillary and allowed to polymerize at RT. Finally, the sample was pushed out and mounted in the sample chamber of the microscope at 37°C in 5% CO_2/95% air for imaging. This method was also used to characterize the interaction of FITC- or RITC-labeled polymeric nanoparticles with the spheroids. LSFM images were deconvolved using IMARIS Professional software (https://imaris.oxinst.com/).

Time-lapse video microscopy

We used video microscopy to evaluate the interspecies interaction between hCMEC/D3 and rat microglia cells. For this, these two cells were co-cultured on low-attachment agarose coated 96-well plates or CellCarrier Spheroid ULA 96-well plates with special optical bottom to form spheroids (see above). Cultures were kept at 37°C in humidified 5% CO_2/95% air within a mini-incubator attached to the microscope stage. Time-lapse videos were recorded in both phase-contrast optical, and fluorescence modes using Alexa® Fluor 488 and 594 and DAPI

nuclear staining by using the InCell Analyzer 2000. Twenty-thirty individual cells were chosen in every starting microscopic image for cell-cell interactions. Images were acquired with a 10x objective at the end of each illumination period (every 10 min) for 24 h. Obtained digital images and image sequences were translated into a video format (AVI).

Total RNA sequencing and data processing

At the end of day 5, total RNA was extracted from BBB spheroids using a T-series Ultraclear 1.5 mL Microcentrifuge tube (Scientific Specialties, Inc., Lodi, CA, USA). The spheroid pellet was immersed in 500 µL of TRIzol (Invitrogen, Carlsbad, CA, USA) following the manufacturer's instructions and stored at -80°C until further use. Samples were analysed in triplicates for RNA-Seq analysis. RNA-Seq libraries were constructed by using Illumina HiSeq 2500 Stranded Total RNA TruSeq RNA Library Preparation Kit v2 (Illumina, San Diego, CA, USA) and sequenced on the Illumina Nova Seq 6000 platform in the SR 50bp and barcode (Illumina). Total RNA-seq was performed from three replicates of 1-cell (only endothelial) and 5-cell spheroids.

For gene expression analyses, trimmed reads with cutadapt were aligned to the reference genome (hg38UCSCassembly) using FASTQC version 0.11.5 (uses cutadapt version 1.10, Brabraham Bioinformatics, Cambridge, UK) and Tophat2 version 2.1.0 (uses Bowtie2 version 2.2.6, Johns Hopkins University, Baltimore, MD, USA), with default parameters and Ref Seq annotation (genome-build GRCh38.p9). The distribution of alignments was analysed using Cufflinks version 2.2.1 (Trapnell Lab, University of Washington, Seattle, WA, USA) and fragments per kilo base of exon model per million reads mapped values were quantile normalized. The quality control of the sequenced data (quality of all sequenced bases, trimming and mapping statistics in all reads) was evaluated using FASTQC version 0.11.5 (**Tables S1-S3**). The minimal quality threshold was set to 20 (phred scale) and the selected TruSeq RNA adapter sequence was: AGATCGGAAGAGC. The quality scores are presented as Phred values (10 log10P base call is wrong), i.e., values higher than 30 indicate a probability of less than 10^{-3} of an incorrect base call (**Figure S8**).

Only unique mapped reads were counted to genes, using 'HTSeq-count' package version 0.6.1 with 'union' mode. Normalization and differential expression analyses (**Table S8**) were conducted using DESeq2 R package version 1.18.1. The reads were mapped to the Homo sapiens (human) genome assembly *GRCh38* (hg38) from Genome Reference Consortium (ftp://ftp.ensembl.org/pub/release-96/fasta/homo_sapiens/) using Tophat2 version 2.1.0 (uses

Bowtie2 version 2.2.6), with up to maximum of 3 mismatches allowed per read, the minimum and maximum intron sizes were set to 70 and 50,000, respectively, and an annotation file was provided to the mapper (**Figure S9**). Replicates were analyzed by the similarity between the suggested replicates and explore the relations between the samples, heatmaps and Principal Component Analysis (PCA) plots were generated by a plot that span(s) the samples in 2D plane by their first two principal components (**Figure S6**).

Protein expression analysis

Five-cell spheroids were collected and washed with PBS several times and lysed by adding a NP-40 lysis buffer (Thermo Fisher Scientific) to conduct Western Blot analysis. Cell lysates were centrifuged (16,800g, 4°C) in a table-top centrifuge (Eppendorf, Hamburg, Germany) and stored at −80°C until use. Protein concentrations were determined by Bradford protein assay (Bio-Rad Laboratories) and SDS-PAGE was performed according to standard protocols. In each lane, total protein was loaded, and 10% or 15% SDS-PAGE gels were used. Gels were transferred to nitrocellulose membranes (GE Healthcare Life Sciences, Marlborough, MA, USA), blocked with 5% w/v non-fat milk (Sigma-Aldrich) for 1 h at RT, washed and incubated with the selective potentially associated primary antibody for overnight at 4^0C (see above for antibodies list). Membranes were washed and incubated with the respective secondary HRP conjugate antibody (Bio-Rad Laboratories) for chemiluminescence analysis with an Image Quant LAS 4000 camera (GE Healthcare Life Sciences). The following primary antibodies were used at a concentration of 1:500: (i) βIII-tubulin antibody, (ii) GFAP, (iii) Iba-1/AIF-1 and (iv) VE-cadherin.

The nanoparticles

In this work, we utilized different polymeric, metallic and carbon nanoparticles to assess their permeability in 5-cell spheroids.

Polymeric nanoparticles

Different polymeric NPs were obtained by the self-assembly of amphiphilic graft copolymers of chitosan (CS), poly(vinyl alcohol) (PVA) and hydrolyzed galactomannan (hGM) with poly(methyl methacrylate) (PMMA). The copolymers were synthesized by the free radical graft polymerization of methyl methacrylate (MMA) initiated by cerium(IV) ammonium nitrate (CAN) in acid aqueous medium. For this, CS, PVA or hGM (0.4 g) was dissolved in nitric acid solution in water (0.05 M). Then, tetramethylethylenediamine (0.18 mL) was diluted in distilled water (50 mL) in a closed round-bottom flask protected from light. Then, both

solutions were degassed separately by sonication for 30 min (Elmasonics S 30, Elma, Singen, Germany), mixed, purged with N_2 gas for 30 min at room temperature, and heated to 35 °C, and the corresponding amount of MMA (according to the desired weight feed ratio) was directly poured into the solution. Finally, a CAN solution (0.66 g in 2 mL of degassed water) was added, and the reaction was carried out under a N_2 environment (3-6 h, 35 °C). The polymerization was finalized by the addition of hydroquinone (0.132 g). Reaction crudes were dialyzed against water (regenerated cellulose dialysis membranes; MWCO, 3500 Da) in 100-fold volume of the dialyzed solution and freeze-dried (72−96 h). Products were stored at 4 °C until use (Moshe Halamish et al., 2019; Noi et al., 2018; Schlachet and Sosnik, 2019; Zaritski et al., 2019).

Metallic nanoparticles

Au NPs (diameter of 10 nm, Sigma-Aldrich) and Ag NPs (diameter of 60 nm) synthesized from silver nitrate by reduction with sodium borohydride and stabilization with sodium citrate (all supplied by Sigma-Aldrich) (Bastús et al., 2014; Quintero-Quiroz et al., 2019) were utilized as prototypes of metallic NPs.

Carbonaceous nanoparticles

We used graphene nanoplatelets (diameter of ~5 μm and thickness of ~100 nm, GNN P0205, Ants Ceramics Pvt. Ltd., Vasai-Virar, India) and alkaline carbon dots produced by the reaction of acetone with sodium hydroxide (Hou *et al.*) (Hou et al., 2015) Briefly, NaOH (8 g, Sigma-Aldrich) was mixed with acetone (40 mL, Bio-Lab Ltd., Netanya, Israel) under magnetic stirring (1 h). Then, the mixture was stored at ambient air and RT (5 days) and the pH adjusted to 7 with HCl solution (1 M, Bio-Lab Ltd.) was added to adjust the pH to be neutral. Carbon dots were separated by centrifugation and washed with water several times, and the product dried at 100 °C for 12 h.

The size (hydrodynamic diameter, D_h) and size distribution (polydispersity, PDI) of the different nanoparticles before the biological studies were measured by dynamic light scattering (DLS, Zetasizer Nano-ZS, Malvern Instruments, Malvern, UK) in 10 mm quartz cuvettes using a He-Ne laser (673 nm) as light source at a scattering angle of 173°, at 25°C. Data were analyzed using CONTIN algorithms (Malvern Instruments). The surface charge was estimated by measuring the zeta-potential (Z-potential) by laser Doppler micro-electrophoresis in the Zetasizer Nano-ZS. Each value is expressed as mean ± S.D. of at least three independent samples, while each DLS or Z-potential measurement is an average of at least seven runs. For

biological studies, copolymers were fluorescently-labeled with FITC or RITC, both from Sigma-Aldrich (Moshe Halamish et al., 2019; Noi et al., 2018; Schlachet and Sosnik, 2019; Zaritski et al., 2019). The properties of the NPs used in this work are summarized in **Table S7**. Before use, NPs were diluted under sterile conditions and mixed with the corresponding culture medium to the final desired concentration.

Statistical Analysis

RNA-Seq data to compare between spheroid groups was obtained from three biological replicates. Wald test parameters were used for pairwise comparisons. The statistical analysis was conducted and the log2 fold change and the adjusted p-values (p_{adj}) were indicated for significantly upregulated and downregulated genes; $p_{adj} < 0.05$ was considered statistically significant. The differential expression analysis was conducted using 'DESeq2' R software. The Zen software was used to evaluate CLSFM and LSFM images. In some cases, the TIFF images acquired with IMARIS software were imported for subsequent measurement and analysis. Results are expressed as mean ± S.D. of three experimental replicates performed under the same conditions (n = 3), unless otherwise specified. All cellular measurements and subsequent analyses were performed in a blinded manner and cell counts and image processing for all experimental conditions were carried out in triplicate. CT values and normalized gene expression values were taken after analysis and the data were exported to Excel (Microsoft, Seattle, WA, USA) spreadsheet software for expression units and S.D. analysis.

References

Bastús, N.G., Merkoçi, F., Piella, J., and Puntes, V. (2014). Synthesis of Highly Monodisperse Citrate-Stabilized Silver Nanoparticles of up to 200 nm: Kinetic Control and Catalytic Properties. Chemistry of Materials *26*, 2836-2846.

Beaudoin, G.M., 3rd, Lee, S.H., Singh, D., Yuan, Y., Ng, Y.G., Reichardt, L.F., and Arikkath, J. (2012). Culturing pyramidal neurons from the early postnatal mouse hippocampus and cortex. Nat Protoc *7*, 1741-1754.

Brissette, C.A., Kees, E.D., Burke, M.M., Gaultney, R.A., Floden, A.M., and Watt, J.A. (2013). The multifaceted responses of primary human astrocytes and brain microvascular endothelial cells to the Lyme disease spirochete, Borrelia burgdorferi. ASN Neuro *5*, 221-229.

Douglas, W.H., and Elser, J.E. (1972). A method for in situ embedding of cultured cells grown on plastic surfaces. In Vitro *8*, 26-29.

Moshe Halamish, H., Trousil, J., Rak, D., Knudsen, K.D., Pavlova, E., Nyström, B., Štěpánek, P., and Sosnik, A. (2019). Self-assembly and nanostructure of poly(vinyl alcohol)-graft-poly(methyl methacrylate) amphiphilic nanoparticles. Journal of Colloid and Interface Science *553*, 512-523.

Hou, H., Banks, C.E., Jing, M., Zhang, Y., and Ji, X. (2015). Carbon Quantum Dots and Their Derivative 3D Porous Carbon Frameworks for Sodium-Ion Batteries with Ultralong Cycle Life. Advanced Materials *27*, 7861-7866.

Johnstone, B., Hering, T.M., Caplan, A.I., Goldberg, V.M., and Yoo, J.U. (1998). In vitro chondrogenesis of bone marrow-derived mesenchymal progenitor cells. Exp Cell Res *238*, 265-272.

Murray, A.B., Schulze, H., and Blauw, E. (1991). In situ embedding of cell monolayers cultured on plastic surfaces for electron microscopy. Biotech Histochem *66*, 269-272.

Neuhaus, A.A., Couch, Y., Sutherland, B.A., and Buchan, A.M. (2017). Novel method to study pericyte contractility and responses to ischaemia in vitro using electrical impedance. J Cereb Blood Flow Metab *37*, 2013-2024.

Noi, I., Schlachet, I., Kumarasamy, M., and Sosnik, A. (2018). Permeability of Novel Chitosan-g-Poly(Methyl Methacrylate) Amphiphilic Nanoparticles in a Model of Small Intestine In Vitro. Polymers (Basel) *10*, 478.

Phillips, D.M. (1998). Electron microscopy: use of transmission and scanning electron microscopy to study cells in culture. Methods Cell Biol *57*, 297-311.

Quintero-Quiroz, C., Acevedo, N., Zapata-Giraldo, J., Botero, L.E., Quintero, J., Zárate-Triviño, D., Saldarriaga, J., and Pérez, V.Z. (2019). Optimization of silver nanoparticle synthesis by chemical reduction and evaluation of its antimicrobial and toxic activity. Biomaterials Research *23*, 27.

Saura, J., Tusell, J.M., and Serratosa, J. (2003). High-yield isolation of murine microglia by mild trypsinization. Glia *44*, 183-189.

Schlachet, I., and Sosnik, A. (2019). Mixed Mucoadhesive Amphiphilic Polymeric Nanoparticles Cross a Model of Nasal Septum Epithelium in Vitro. ACS Applied Materials & Interfaces *11*, 21360-21371.

Seibenhener, M.L., and Wooten, M.W. (2012). Isolation and culture of hippocampal neurons from prenatal mice. J Vis Exp *65*, 3634.

Zaritski, A., Castillo-Ecija, H., Kumarasamy, M., Peled, E., Sverdlov Arzi, R., Carcaboso, Á.M., and Sosnik, A. (2019). Selective Accumulation of Galactomannan Amphiphilic Nanomaterials in Pediatric Solid Tumor Xenografts Correlates with GLUT1 Gene Expression. ACS Applied Materials & Interfaces *11*, 38483-38496.